Intercorrelated random fields with bounds and the Bayesian identification of their parameters: Application to linear elastic struts and fibers

H. Rappel[a,b], M. Girolami[a,c], L.A.A. Beex[d,*]

[a] *The Alan Turing Institute*
[b] *College of Engineering Mathematics and Physical Sciences, University of Exeter*
[c] *Department of Engineering, University of Cambridge*
[d] *Institute of Computational Engineering, Faculty of Science, Technology and Medicine, University of Luxembourg*

Abstract

Many materials and structures consist of numerous slender struts or fibers. Due to the manufacturing processes of different types of struts and the growth processes of natural fibers, their mechanical response frequently fluctuates from strut to strut, as well as locally within each strut. In associated mechanical models each strut is often represented by a string of beam elements, since the use of conventional 3D finite elements renders the simulations computationally inefficient. The parameter input fields of each string of beam elements are ideally such that the local fluctuations and fluctuations between individual strings of beam elements are accurately captured. The goal of this study is to capture these fluctuations in several intercorrelated bounded random fields. Two formulations to describe the intercorrelations between each random field, as well as the case without any intercorrelation, are investigated. As only a few sets of input fields are available (due to time constraints of the supposed experimental techniques), the identification of the random fields' parameters is ill-posed. A probabilistic identification approach based on Bayes' theorem is employed to treat the ill-posedness, as well as the involved uncertainties.

Keywords: Bayesian inference, Intercorrelated random fields, Copula, Intrinsic coregionalization model, Semiparametric latent factor model, Beams

1. Introduction

Many materials and structures consist of numerous slender struts or fibers. Associated mechanical models frequently employ a string of beam elements to represent each strut [1] or fiber [2]. Often, the geometry of each strut or fiber is somewhat different (e.g. struts in open-cell metal foams [1] and metal printed lattices [3] due to the manufacturing processes, and fibers in flora [4] and fauna [5] due to the growth processes). In this study, these variations are treated in five intercorrelated random fields that are used as the spatially varying parameter fields of the beam representation. The aim is to identify the parameters of the intercorrelated random input fields, given that only a few strut geometries are known, so that not only the reaction forces and reaction moments, varying between struts, but also the spatially fluctuating center line displacements are properly captured. Because the experimental characterization of strut geometries is typically time-consuming, only a few geometries are considered. This makes the identification problem ill-posed and introduces substantial uncertainties. This is treated in this contribution with Bayesian inference.

The framework presented in this contribution is an extension of the authors' former study [6] in which Bayesian inference was used to identify the parameters of a single random field. Similar as in the present study, the random field description is bounded, so that bounds of physical quantities are incorporated. The current contribution extends the previous one to several random fields with mutual correlations. Consequently, the parameters to be identified are the parameters of a univariate probability density function for each random field, the parameters governing the spatial correlations, as well as the parameters that define the correlation between the fields. Once these parameters are identified, realizations from the random fields can be used as input fields for forward problems (which is not considered in this contribution).

*Corresponding author
Email address: lars.beex@uni.lu (L.A.A. Beex)

Gaussian processes and copula theory. This study heavily relies on the concept of Gaussian processes/fields (GPs)[1]. GPs are well-known and the related theories are covered in classical text books [7–10]. Also in the field of mechanics, GPs are regularly utilized [11–14].

Simply stated, a GP is a generalization of a multivariate Gaussian distribution over an infinite-dimensional function space [8]. This implies that any finite-dimensional realization of a GP is a multivariate Gaussian distribution with a given mean and covariance matrix. As the univariate marginal probability density functions (PDFs) in GPs are Gaussian distributions (with the same mean and variance), they are strictly speaking not applicable to many physical problems, because physical quantities are often bounded (e.g. Young's modulus is positive). This issue can be avoided by combining GPs with the copula theory in order to create a random field with bounds [15, 16].

According to the copula theory [17], one can write the dependency between several random variables independent of their univariate marginal distributions. A copula function achieves this by combining the marginal univariate cumulative distribution function (CDF) of each random value and producing a joint multivariate distribution function. Using the copula theorem a multivariate Gaussian distribution can be written as a combination of univariate Gaussian distributions linked with each other through a Gaussian copula [18]. The Gaussian copula then only dictates the dependency/correlation structure. This implies that the marginal univariate Gaussian distribution of a GP can be replaced by a non-Gaussian one, yielding a joint distribution with a Gaussian correlation structure and a non-Gaussian (e.g. bounded) univariate marginal distribution.

This logic is employed by Jaimungal and Ng [15] to create kernel-based copula processes where kernel functions [7] are employed to describe the covariance between pairs of random variables. The general definition of a copula process is given by Wilson and Ghahramani [16] who have not limited themselves to the Gaussian copula. Rappel et al. [6] used the same concept to bound a random field of effective Young's moduli in polycrystalline materials.

Multi-output Gaussian processes. In the current contribution, five parameter fields are simultaneously considered. The first and most simplistic approach would be to consider each parameter field as an independent random process/field. However, this may lead to the loss of information, as the fields may be mutually correlated.

Multi-output Gaussian processes (MOGPs) are used to model dependencies between outputs in a wide variety of fields: geostatistics [19, 20], machine learning [21–25], emulation of computer codes/models (simulation codes) [26–29] as well as numerical predictions of physical systems [30, 31]. Ardent et al. [32] have furthermore employed multiple response (multi-output) systems to improve the identifiability of calibration parameters based on the fact that multiple responses can provide additional information if the responses depend on the same set of calibration parameters. They have used the multi-output Gaussian process as a surrogate model that represents the computer model. Ardent et al. [32] have demonstrated the capabilities of the framework to describe the deflection of a simply supported beam [13] where the quantities of interest were the center line displacement and the strain in center of the beam. MOGPs are also employed by Richardson et al. [33], who have used MOGP regression to forecast the degradation of batteries. Extensive reviews on MOGPs are given in [34] and [35].

The aforementioned studies generally use MOGPs for nonparametric regression and data prediction. However, in the current contribution they are used to describe (bounded) fields of geometrical and mechanical parameters with spatial correlations as well as correlation between the different fields.

Bayesian parameter identification. The Bayesian paradigm is employed in the current contribution to identify the parameters of the random fields/PDFs. A probabilistic framework based on Bayesian inference (BI) makes it possible to quantify the modeling uncertainties of the identified parameters. In this paradigm the user's a-priori knowledge about the parameters, which is represented by a probability distribution, is updated by observations through Bayes' theorem (formula).

Numerous studies in mechanics have used the concept of Bayesian inference for parameter identification. Some examples are the works of Isenberg [36], Alvin [37], Beck and Katafygiotis [38], Marwala and Sibusiso [39], Gogu et al. [40], Lai and Ip [41], Daghia et al. [42], Nichols et al. [43] and Gogu et al. [44] for elasticity, the studies of Most [45], Rappel et al. [14, 46], Zhang et al. [47] and Zhang and Needleman [48] for elastoplasticity and plasticity the studies of Muto and Beck [49], Liu and Au [50], Fitzenz et al. [51], Hernandez et al. [52] and Rappel et al. [53] for other material descriptions involving dissipation. The paradigm is furthermore employed by Rappel and Beex [54] to identify material parameter distributions/PDFs with a limited number of observations. Similarly, Mohamedou et al. [55] have employed BI for the identification of the resin's Young's modulus in non-aligned short fiber composites.

[1]Note that in this contribution a random field is a stochastic process in (Euclidean) space and using the term 'field' or 'process' will not change our definitions.

Furthermore, frameworks based on BI and GP are provided by Koutsourelakis to identify spatially varying parameters for perfect plasticity [56] and elasticity [57]. The framework in [56] is based on a representation of GPs in terms of basis functions [9]. Alternatively, [57] applies BI directly on the finite element (FE) discretization in which the stiffness tensor (i.e the spatially varying properties) is constant within each finite element. Hence, the components of the element-wise tensors are the random variables of the posterior (i.e. the number of dimensions of the posterior scales with the number of FEs). Another study in which BI is used to identify spatially varying material properties is the one of Uribe et al. [58] in which BI is employed for the identification of a hydraulic conductivity field, represented as a GP with a Karhunen-Loève expansion. Vigliotti et al. [59] have furthermore employed BI to identify spatially fluctuating fields of Young's moduli and Poisson's ratios. In their work the parameter fields are modeled using B-splines. Model selection is employed to select the order of the B-splines. The framework of Rappel et al. [6] furthermore employs copula Gaussian process and BI to identify the spatially varying homogenized Young's modulus field of a columnar polycrystalline material. Savvas et al. [60] have proposed a Bayesian framework to identify the parameters fields of apparent material properties of two-phase composites.

Outlook. The remainder of this paper is organized as follows. Section 2 discusses the general concept of this study in more detail from a mechanics point of view. Section 3 presents the mechanical models employed in this study. In Section 4 we briefly discuss the essential theoretical concepts to model the input fields as random fields. Section 5 provides a concise description of Bayesian inference. Section 6 presents the identification of the random fields employed using the concepts discussed in Section 4. In Section 7 we discuss the result of this study and finally conclusions are presented in Section 8.

2. The approach in a nutshell

This short section describes the main workflow in simple words. The starting assumption is that (slightly varying) geometries of six struts are accurately known (left column in Fig. 1(a)). Accurate material descriptions for these struts (isotropic linear elasticity), including the associated parameter values, are also assumed to be available. Five types of virtual experiments are performed on these six struts using (computationally expensive) simulations with conventional 3D hexahedral finite elements (FEs). Consequently, the center line displacements and rotations, as well as the reaction forces and moments of these struts are predicted for five types of applied deformations. Note that different deformation modes are applied, as each strut is exposed to an unknown combination of axial elongation, axial torsion and bending around different axes in the forward simulations (not considered in this contribution).

After the results of the FE simulations are computed and processed, the same fluctuating center line displacements are to be predicted by the beam representation of each strut; a string of perfectly aligned beam elements. This is accomplished by deterministically identifying five input fields for the beam representation, independently for each of these six struts (remainder of Fig. 1(a)). This deterministic identification problem of a least squares type is tackled with a conjugate gradient framework that minimizes the difference between the locally fluctuating center line displacements of the accurate simulations and the beam simulations.

After the five input fields of the beam representation for each of the six struts are deterministically identified, the probabilistic part of this contribution commences (Fig. 1(b)). Each set of five input fields is considered to be a single realization of a random field/process (in practice a multivariate PDF) and the (uncertainties of the) parameters of this random field/process are identified using Bayesian inference. Each field is assumed to be a Gaussian-copula field so that bounds of the parameters are incorporated. The intercorrelations between these fields are modeled by three different formulations and the probabilistic identification is performed separately for each formulation (see Sections 4 and 6).

Finally, the approach is verified (Fig. 1(c)). This is accomplished by first generating another 994 strut geometries and virtually exposing them to the five deformation modes with the FE simulations using hexahedral finite elements (left in Fig. 1(c)). On the other hand, 994 sets of five input fields are generated from the identified random fields/processes and used as parameter fields for the beam simulations (right in Fig. 1(c)). This is repeated three times; for the three different formulations to describe the intercorrelation between the fields (not shown in Fig. 1(c)). The center line displacements of the FE simulations are compared with the center line displacements of the beam simulations in order to compare the abilities and inabilities of the three different methods of describing the intercorrelation between the fields.

Note that in the current contribution, the geometries are artificially generated so that not only six struts can virtually be tested, but many more. This enables a comparison between the beam results (employing the random field descriptions) and the results of numerous FE simulations using 3D hexahedral finite elements to accurately describe the strut geometries.

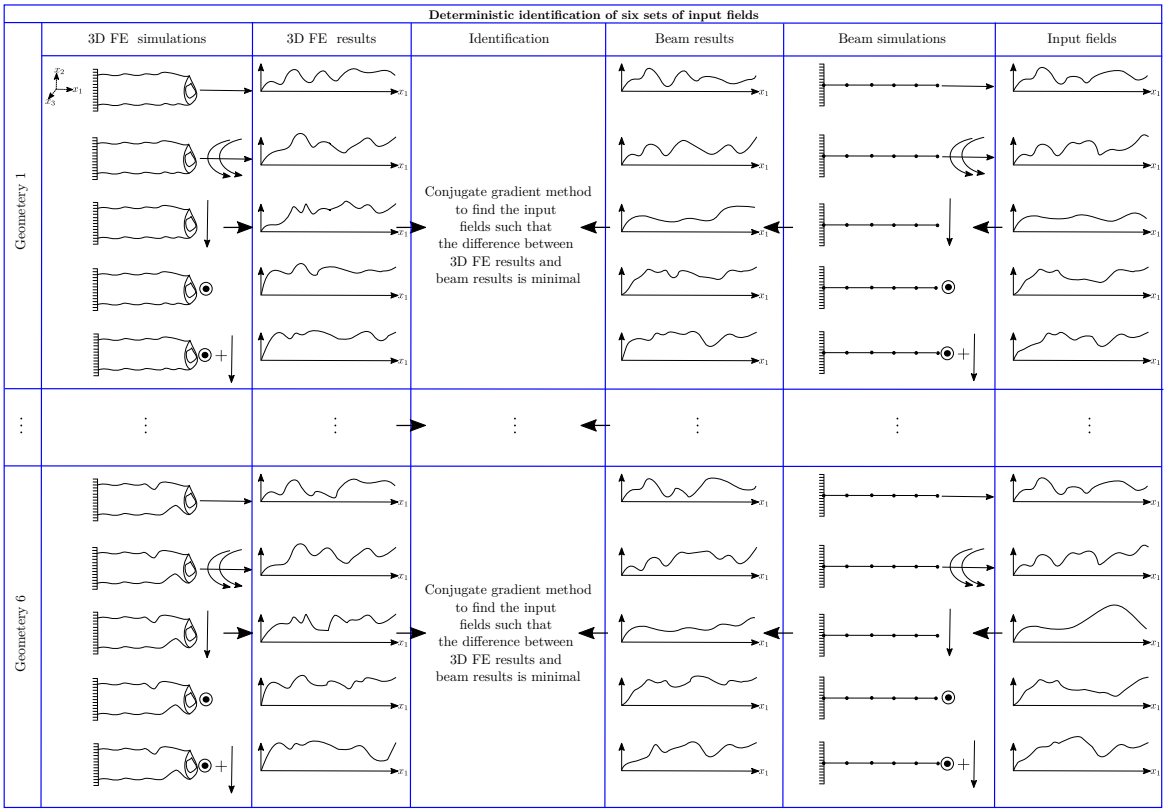

(a)

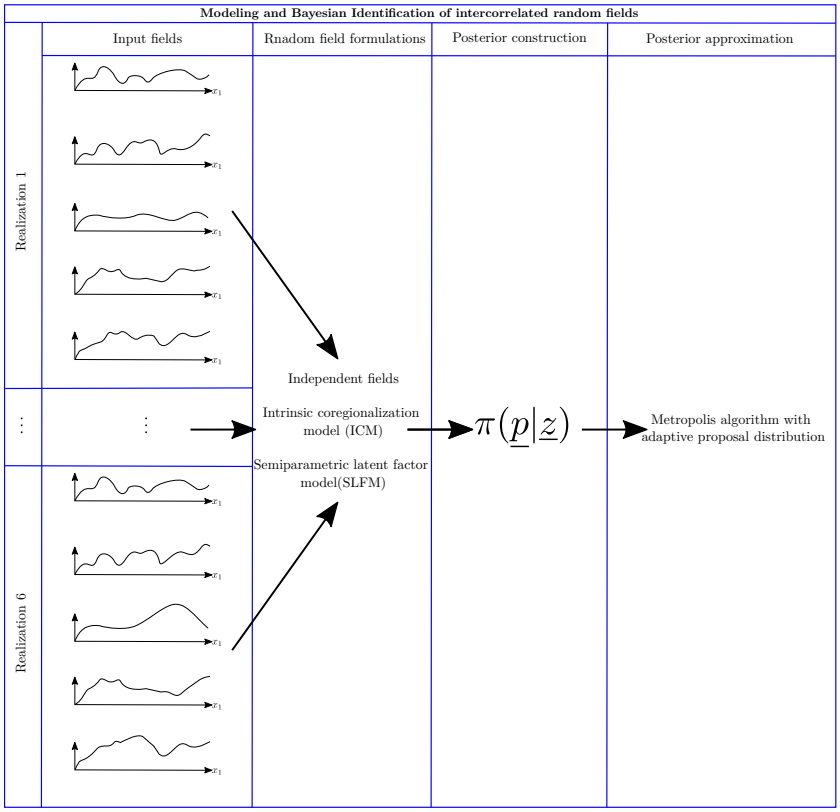

(b)

Figure 1: Illustration of the general concept of the study. (a) Deterministic identification of six input fields (b) modeling input fields as intercorrelated random fields and their identification (c) verification.

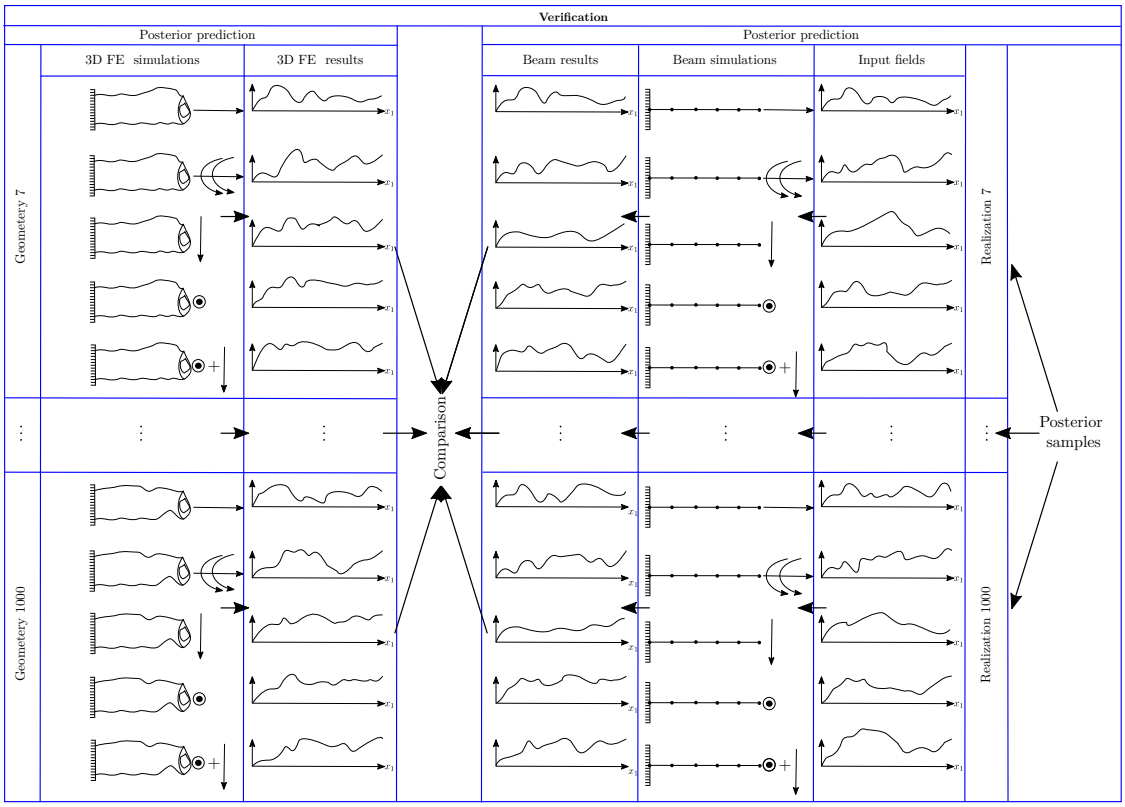

(c)

Continued Figure 1: Illustration of the general concept of the study. (a) Deterministic identification of six input fields (b) modeling input fields as intercorrelated random fields and their identification (c) verification.

3. Mechanical simulations

In this section, the two types of linear elastic mechanical simulations are discussed. The first type of simulations (from here onwards referred to as 'finite element simulations' or 'FE simulations') uses hexahedral (eight-node) finite elements in order to accurately represent the spatially fluctuating geometries. These simulations are used to assess the 'accurate' mechanical responses of each strut geometry. In the first subsection the finite element approach of this type of simulation is discussed, whereas the artificial generation of the fluctuating geometries, together with the mesh generation and the applied deformations, is discussed in the second subsection.

The second type of mechanical simulations uses a string (i.e. series) of Euler-Bernoulli beam elements to describe the mechanical responses. These beam simulations are discussed in the third subsection (and also in appendix A of [61]). The input parameters of each beam element are to be identified such that the beam responses match the responses predicted by the FE simulations. To this end, the input parameters of each beam element are considered as (deterministic) variables in a least-squares problem that is solved using the conjugate gradient method. The fourth subsection therefore discusses the adjoint method (see e.g. [62, 63]) to efficiently evaluate the beam simulation's gradient with respect to the input parameters.

3.1. Finite element simulations

The accurate FE simulations employ 3D trilinear hexahedral (i.e. eight-node) finite elements with eight Gauss quadrature points to accurately represent each strut. Because isotropic linear elasticity is considered, the following expression for the Cauchy stress, $\boldsymbol{\sigma}(\vec{X})$ ($\vec{X}$ denotes the location of a material point in the undeformed configuration), is employed:

$$\boldsymbol{\sigma} = {}^4\mathbf{C} : \boldsymbol{\epsilon}, \tag{1}$$

where ${}^4\mathbf{C}$ denotes the constant (i.e. independent of location and deformation) fourth-order stiffness tensor of which each component is expressed in terms of a single Young's modulus and a single Poisson's ratio. For all finite element simulations, Young's modulus is set to 1 and Poisson's ratio to 0.3. Furthermore, $\boldsymbol{\epsilon}(\vec{X})$ denotes the infinitesimal strain tensor, which can be expressed as follows in the discretized setting:

$$\boldsymbol{\epsilon} = \frac{1}{2}\left(\vec{\nabla}\underline{N}^T\underline{\vec{u}} + \left(\vec{\nabla}\underline{N}^T\underline{\vec{u}}\right)^T\right), \tag{2}$$

where $\vec{\nabla} = \frac{\partial}{\partial \vec{X}}$ denotes the gradient operator, $\underline{N}(\vec{X})$ the column with shape functions, $\underline{\vec{u}}$ the column with the nodal displacement vectors and superscript T the transpose.

Applying the method of weighted residuals to the following strong form without the consideration of body forces:

$$\vec{\nabla} \cdot \boldsymbol{\sigma} = \vec{0}, \tag{3}$$

and subsequently the divergence theorem, some symmetry and algebra, eventually yields the following system of linear vector equations:

$$\int_V \vec{\nabla}\underline{N} \cdot {}^4\mathbf{C} \cdot (\vec{\nabla}\underline{N})^T \, dV \cdot \underline{\vec{u}} = \int_S \underline{N}\,\vec{t}\, dS, \tag{4}$$

where V and S denote the undeformed volume and surface of the discretized domain, respectively, and $\vec{t}(\vec{X})$ denotes the traction applied at the surface. This system is numerically integrated using eight Gauss quadrature points per 3D trilinear hexahedral element and written as a system of linear scalar equations. After partitioning to account for Dirichlet boundary conditions, it is solved to determine the unknown nodal displacement components.

3.2. Introduced randomness

In this short subsection, more details of the finite element simulations are discussed. All struts are hollow and have a length of 100 and an outer radius of roughly 2 and an inner radius of roughly 1. The mesh contains 400 elements in the axial direction, 52 in angular direction and 4 in radial (i.e. thickness) direction. This element grid is chosen such that 4 elements are used over the wall thickness, while each element has roughly the shape of a cube (with a volume of approximately $0.25 \times 0.25 \times 0.25$). In total, 83200 elements and 104260 nodes are involved in each simulation.

The randomness is introduced by randomly selecting 30 to 50 axial locations per strut. For each of these locations, the strut's cross section varies: 1) the outer and inner radii are independently selected from uniform distributions with bounds [1.9, 2.1] and [0.9, 1.1], respectively, and 2) the center of each cross section is not located on top of the strut's axis, but randomly varied with a maximum distance of 0.05 from the strut's axis. Between these 30 to 50 axial locations, the cross section is linearly interpolated and the nodal locations are slightly adjusted in the axial direction to accurately represent the strut's geometry.

Each strut is exposed to five different deformation modes by prescribing all the displacement components of the end nodes (see the left column in Figs. 1(a) and 1(c)). In the first simulation, the nodes at one end are displaced with a distance of 0.1 in the axial direction. Torsion is prescribed in the second simulation by displacing the nodes at one end with a rotation of 0.5° around the axial direction. In the other three simulations, the nodes at one end are displaced with a distance of 0.1 orthogonal to the axial direction; once along the x_2-direction, once along the x_3-direction and once along a direction of 45° with respect to the x_2-direction and the x_3-direction. After each simulation, the reaction forces and moments are extracted and the displacement results are post-processed such that the average center line displacement and rotation is available at 400 equally spaced axial locations. The fact that the undeformed center line is not perfectly straight is ignored in the post-processing.

3.3. Beam simulations

Each beam simulation involves a string of 400 Euler-Bernoulli beam elements (with Hermite interpolation). The undeformed center line of each string is a perfectly straight line. The hollow cross section of each beam is presented in Fig. 2 and hence, involves 4 input parameters: an outer radius (r_o) and three distances that govern the internal shape (r_a, r_b and r_c). These 4 parameters, together with Poisson's ratio, are the parameters that are varied from beam element to beam element in order to match the fluctuations predicted by the 'accurate' FE simulations (described in the previous two subsections). Young's modulus is constant, since it is linearly present in the governing equations and can therefore not be used to describe relative changes of the spatially fluctuating center line results.

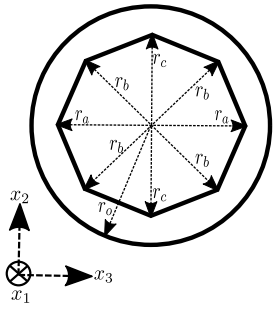

Figure 2: The hollow cross section of each beam element.

Each beam simulation (in the discretized setting) is considered as the following minimization problem:

$$[\underline{u}^{\text{beam}}, \underline{\omega}^{\text{beam}}] = \underset{\underline{u},\underline{\omega}}{\text{argmin}} \quad -\underline{f}_{\text{ext}}^T\underline{u} - \underline{M}_{\text{ext}}^T\underline{\omega} + \sum_{i=1}^{400} E_i(\underline{u},\underline{\omega}), \tag{5}$$

where $\underline{f}_{\text{ext}}$ and $\underline{M}_{\text{ext}}$ denote the columns with external force components and moment components, respectively. $\underline{u}$ and $\underline{\omega}$ denote the columns with displacement components and rotation components, respectively. The elastic energy of a beam element is denoted by E and is expressed as follows:

$$E = \frac{Y}{2}\int_V \left(\epsilon_{ae1} + \epsilon_{b2} + \epsilon_{b3}\right)^2 + \frac{\gamma_{12}^2 + \gamma_{13}^2}{2(1+\nu)} dV, \tag{6}$$

where V, Y and ν denote the beam's reference volume, Young's modulus and Poisson's ratio, respectively. The axial strain due to uniform elongation (in the x_1-direction) is denoted by ϵ_{ae1}, the axial strain due to bending around the x_2-direction by ϵ_{b2} and the axial strain due to bending around the x_3-direction by ϵ_{b3}. γ_{12} and γ_{13} denote the shear strains occurring due to axial torsion. Note that the directions are presented in Figs. 1(a) and 2.

By incorporating the linear interpolation of the axial displacement, the linear interpolation of the rotation around the axial direction and the axial strains due to bending expressed in terms of the curvatures, Eq. (6) can be expressed as follows:

$$E = \frac{Y}{2}\int_V \left(\frac{u_{1/b} - u_{1/a}}{L} - x_3\frac{\partial^2 u_3}{\partial (x_1)^2} - x_2\frac{\partial^2 u_2}{\partial (x_1)^2}\right)^2 + \left(\frac{\omega_{1/b} - \omega_{1/a}}{L}\right)^2 \frac{x_2^2 + x_3^2}{2(1+\nu)} dV, \tag{7}$$

where subscripts a and b are used to distinguish the two nodes of a beam element. L denotes the undeformed (axial) length of the beam element. Again, subscripts 1, 2 and 3 refer to the directions as presented in Figs. 1(a) and 2.

Hermite interpolation is employed to relate transversal center line displacement components $u_2(x_1)$ and $u_3(x_1)$ to the relevant nodal displacements and rotations. A third-order polynomial is employed for $u_2(x_1)$ and a third-order polynomial is used for $u_3(x_1)$. The coefficients of the polynomial for $u_2(x_1)$ are determined by solving the following system of linear equations:

$$u_2(x_1 = 0) = u_{2/a} \qquad u_2(x_1 = L) = u_{2/b} \qquad \left.\frac{\partial u_2}{\partial x_1}\right|_{x_1=0} = \omega_{3/a} \qquad \left.\frac{\partial u_2}{\partial x_1}\right|_{x_1=L} = \omega_{3/b}, \tag{8}$$

and the coefficients of the polynomial for $u_3(x_1)$ are determined by solving the following system of linear equations:

$$u_3(x_1 = 0) = u_{3/a} \qquad u_3(x_1 = L) = u_{3/b} \qquad \left.\frac{\partial u_3}{\partial x_1}\right|_{x_1=0} = -\omega_{2/a} \qquad \left.\frac{\partial u_3}{\partial x_1}\right|_{x_1=L} = -\omega_{2/b}. \tag{9}$$

Finally, the volume integral in Eq. (7) must be specified for the cross section of interest (Fig. 2). This yields:

$$E = \frac{Y}{2}\int_0^L \int_{-r_o}^{r_o} \int_{-\sqrt{r_o^2 - x_3^2}}^{\sqrt{r_o^2 - x_3^2}} \left(\frac{u_{1/b} - u_{1/a}}{L} - x_3\frac{\partial^2 u_3}{\partial (x_1)^2} - x_2\frac{\partial^2 u_2}{\partial (x_1)^2}\right)^2 + \left(\frac{\omega_{1/b} - \omega_{1/a}}{L}\right)^2 \frac{x_2^2 + x_3^2}{2(1+\nu)} dx_2\, dx_3\, dx_1 -$$

$$\frac{Y}{2}\int_0^L\int_{-r_a}^{-\frac{r_b}{\sqrt{2}}}\int_{-x_2^I(x_3)}^{x_2^I(x_3)}\left(\frac{u_{1/b}-u_{1/a}}{L}-x_3\frac{\partial^2 u_3}{\partial(x_1)^2}-x_2\frac{\partial^2 u_2}{\partial(x_1)^2}\right)^2+\left(\frac{\omega_{1/b}-\omega_{1/a}}{L}\right)^2\frac{x_2^2+x_3^2}{2(1+\nu)}dx_2\,dx_3\,dx_1-$$
$$\frac{Y}{2}\int_0^L\int_{-\frac{r_b}{\sqrt{2}}}^{0}\int_{-x_2^{II}(x_3)}^{x_2^{II}(x_3)}\left(\frac{u_{1/b}-u_{1/a}}{L}-x_3\frac{\partial^2 u_3}{\partial(x_1)^2}-x_2\frac{\partial^2 u_2}{\partial(x_1)^2}\right)^2+\left(\frac{\omega_{1/b}-\omega_{1/a}}{L}\right)^2\frac{x_2^2+x_3^2}{2(1+\nu)}dx_2\,dx_3\,dx_1-$$
$$\frac{Y}{2}\int_0^L\int_{0}^{\frac{r_b}{\sqrt{2}}}\int_{-x_2^{III}(x_3)}^{x_2^{III}(x_3)}\left(\frac{u_{1/b}-u_{1/a}}{L}-x_3\frac{\partial^2 u_3}{\partial(x_1)^2}-x_2\frac{\partial^2 u_2}{\partial(x_1)^2}\right)^2+\left(\frac{\omega_{1/b}-\omega_{1/a}}{L}\right)^2\frac{x_2^2+x_3^2}{2(1+\nu)}dx_2\,dx_3\,dx_1-$$
$$\frac{Y}{2}\int_0^L\int_{\frac{r_b}{\sqrt{2}}}^{r_a}\int_{-x_2^{IIII}(x_3)}^{x_2^{IIII}(x_3)}\left(\frac{u_{1/b}-u_{1/a}}{L}-x_3\frac{\partial^2 u_3}{\partial(x_1)^2}-x_2\frac{\partial^2 u_2}{\partial(x_1)^2}\right)^2+\left(\frac{\omega_{1/b}-\omega_{1/a}}{L}\right)^2\frac{x_2^2+x_3^2}{2(1+\nu)}dx_2\,dx_3\,dx_1, \quad (10)$$

where the second and fifth integral are ignored in case $\sqrt{2}r_a = r_b$, and $x_2^I(x_3)$ to $x_2^{IIII}(x_3)$ are expressed as follows:

$$\begin{aligned} x_2^I(x_3) &= \frac{r_b(x_3+r_a)}{\sqrt{2}r_a - r_b}, \quad x_2^{II}(x_3) = \frac{\sqrt{2}r_c - r_b}{r_b}x_3 + r_c, \\ x_2^{III}(x_3) &= \frac{r_b - \sqrt{2}r_c}{r_b}x_3 + r_c, \quad x_2^{IIII}(x_3) = \frac{r_b(r_a - x_3)}{\sqrt{2}r_a - r_b}. \end{aligned} \quad (11)$$

Now the objective function is formulated, the interior extremum theorem is applied in order to solve it, resulting in the following system of linear equations:

$$\begin{bmatrix} \underline{f}_{\text{int}}(\underline{u},\underline{\omega}) \\ \underline{M}_{\text{int}}(\underline{u},\underline{\omega}) \end{bmatrix} = \begin{bmatrix} \underline{f}_{\text{ext}} \\ \underline{M}_{\text{ext}} \end{bmatrix}, \quad (12)$$

with:

$$\underline{f}_{\text{int}} = \sum_{i=1}^{400}\frac{\partial E_i}{\partial \underline{u}} \qquad \underline{M}_{\text{int}} = \sum_{i=1}^{400}\frac{\partial E_i}{\partial \underline{\omega}}. \quad (13)$$

This equation can be rewritten to solve for the final displacement and rotation components (i.e. $\underline{u}^{\text{beam}}$ and $\underline{\omega}^{\text{beam}}$) as follows:

$$\begin{bmatrix} \frac{\partial \underline{f}_{\text{int}}}{\partial \underline{u}} & \frac{\partial \underline{f}_{\text{int}}}{\partial \underline{\omega}} \\ \frac{\partial \underline{M}_{\text{int}}}{\partial \underline{u}} & \frac{\partial \underline{M}_{\text{int}}}{\partial \underline{\omega}} \end{bmatrix} \begin{bmatrix} \underline{u}^{\text{beam}} \\ \underline{\omega}^{\text{beam}} \end{bmatrix} = \begin{bmatrix} \underline{f}_{\text{ext}} \\ \underline{M}_{\text{ext}} \end{bmatrix}. \quad (14)$$

3.4. Adjoint method

The input parameters of each beam element (r_o, r_a, r_b, r_c and ν) are deterministically identified such that the center line displacements and rotations, as well as the reaction forces and moments match those of the finite element simulations for the six struts of consideration. To this end, a least squares problem is considered for each strut in which the objective function, J, quantifies the difference between the center line displacements and rotations during the five applied deformations:

$$\begin{aligned} J(\underline{z}) = &\left(\underline{u}_1^{\text{FE},e} - \underline{u}_1^{\text{beam},e}(\underline{z})\right)^T\left(\underline{u}_1^{\text{FE},e} - \underline{u}_1^{\text{beam},e}(\underline{z})\right) + \left(\underline{\omega}_1^{\text{FE},t} - \underline{\omega}_1^{\text{beam},t}(\underline{z})\right)^T\left(\underline{\omega}_1^{\text{FE},t} - \underline{\omega}_1^{\text{beam},t}(\underline{z})\right) + \\ &\left(\underline{u}_2^{\text{FE},2} - \underline{u}_2^{\text{beam},2}(\underline{z})\right)^T\left(\underline{u}_2^{\text{FE},2} - \underline{u}_2^{\text{beam},2}(\underline{z})\right) + \left(\underline{u}_3^{\text{FE},3} - \underline{u}_3^{\text{beam},3}(\underline{z})\right)^T\left(\underline{u}_3^{\text{FE},3} - \underline{u}_3^{\text{beam},3}(\underline{z})\right) + \\ &\frac{1}{2}\left(\underline{u}_2^{\text{FE},23} - \underline{u}_2^{\text{beam},23}(\underline{z})\right)^T\left(\underline{u}_2^{\text{FE},23} - \underline{u}_2^{\text{beam},23}(\underline{z})\right) + \frac{1}{2}\left(\underline{u}_3^{\text{FE},23} - \underline{u}_3^{\text{beam},23}(\underline{z})\right)^T\left(\underline{u}_3^{\text{FE},23} - \underline{u}_3^{\text{beam},23}(\underline{z})\right), \end{aligned} \quad (15)$$

where column $\underline{z} = \begin{bmatrix}\underline{r}_o^T & \underline{r}_a^T & \underline{r}_b^T & \underline{r}_c^T & \underline{\nu}^T\end{bmatrix}^T$ collects the input parameters of all the beam elements; the variables in the least squares problem. The superscripts again refer to the different directions. Superscripts FE and beam refer to the center line results of the finite element simulations and to those of the beam simulations, respectively. Superscript e refers to axial elongation as the applied deformation mode, superscript t to torsion as the applied

deformation mode, superscript 2 to the deformation mode in which the nodes at one end are displaced in the x_2-direction, superscript 3 to the deformation mode in which the nodes at one end are displaced in the x_3-direction and superscript 23 to the deformation mode in which the nodes at one end are simultaneously displaced in the x_2-direction and the x_3-direction.

Note that the differences between the reaction forces and moments predicted by the FE simulations and the beam simulations are not considered in the objective function, since an initial guess of $\underline{r}_0 = \underline{2}$, $\underline{r}_a = \underline{1}$, $\underline{r}_b = \underline{1}$, $\underline{r}_c = \underline{1}$, $\underline{\nu} = \underline{0.28}$ is sufficient to guarantee a match of the reaction forces and moments within a couple of percent. It is also worth to note that the second term on the right hand side of Eq. (15) (i.e. the one depending on rotations) is not accompanied by a weight factor, even though the magnitude of the rotations is different than the magnitude of the displacements. The reason for the lack of a weight factor is that Poisson's ratio only influences the axial rotations and nothing else. This can be seen in Eq. (6), as Poisson's ratio is only present in the term associated with torsional shear.

As a conjugate gradient approach is employed to minimize the objective function of Eq. (15), the objective function's gradient with respect to the variables ($\frac{\partial J}{\partial \underline{z}}$) must be evaluated. One could apply the method of finite differences to this end, but this requires 2000 beam simulations per gradient evaluation (400 beam elements, five input parameters per beam element). A computationally more efficient alternative is the adjoint (state) method, which requires two additional matrices (in the current notation):

$$\frac{\partial \underline{f}_{\text{int}}}{\partial \underline{z}}, \qquad \frac{\partial \underline{M}_{\text{int}}}{\partial \underline{z}}, \tag{16}$$

which must be evaluated for the beam solution for each of the five applied deformation modes (i.e. (1) $\underline{u}^{\text{beam},e}$ and $\underline{\omega}^{\text{beam},e}$, (2) $\underline{u}^{\text{beam},t}$ and $\underline{\omega}^{\text{beam},t}$, (3) $\underline{u}^{\text{beam},2}$ and $\underline{\omega}^{\text{beam},2}$, (4) $\underline{u}^{\text{beam},3}$ and $\underline{\omega}^{\text{beam},3}$ and finally, (5) $\underline{u}^{\text{beam},23}$ and $\underline{\omega}^{\text{beam},23}$).

In more detail, gradient $\frac{\partial J}{\partial \underline{z}}$ can be expressed as:

$$\begin{aligned}
\left(\frac{\partial J}{\partial \underline{z}}\right)^T = &-2\left(\underline{u}_1^{\text{FE},e} - \underline{u}_1^{\text{beam},e}\right)^T \begin{bmatrix} \frac{\partial \underline{u}_1^{\text{beam},e}}{\partial \underline{u}^{\text{beam},e}} & \frac{\partial \underline{u}_1^{\text{beam},e}}{\partial \underline{\omega}^{\text{beam},e}} \end{bmatrix} \begin{bmatrix} \frac{\partial \underline{u}^{\text{beam},e}}{\partial \underline{z}} \\ \frac{\partial \underline{\omega}^{\text{beam},e}}{\partial \underline{z}} \end{bmatrix} - 2\left(\underline{\omega}_1^{\text{FE},t} - \underline{\omega}_1^{\text{beam},t}\right)^T \begin{bmatrix} \frac{\partial \underline{\omega}_1^{\text{beam},t}}{\partial \underline{u}^{\text{beam},t}} & \frac{\partial \underline{\omega}_1^{\text{beam},t}}{\partial \underline{\omega}^{\text{beam},t}} \end{bmatrix} \begin{bmatrix} \frac{\partial \underline{u}^{\text{beam},t}}{\partial \underline{z}} \\ \frac{\partial \underline{\omega}^{\text{beam},t}}{\partial \underline{z}} \end{bmatrix} - \\
&2\left(\underline{u}_2^{\text{FE},2} - \underline{u}_2^{\text{beam},2}\right)^T \begin{bmatrix} \frac{\partial \underline{u}_2^{\text{beam},2}}{\partial \underline{u}^{\text{beam},2}} & \frac{\partial \underline{u}_2^{\text{beam},2}}{\partial \underline{\omega}^{beam,2}} \end{bmatrix} \begin{bmatrix} \frac{\partial \underline{u}^{\text{beam},2}}{\partial \underline{z}} \\ \frac{\partial \underline{\omega}^{\text{beam},2}}{\partial \underline{z}} \end{bmatrix} - 2\left(\underline{u}_3^{\text{FE},3} - \underline{u}_3^{\text{beam},3}\right)^T \begin{bmatrix} \frac{\partial \underline{u}_3^{\text{beam},3}}{\partial \underline{u}^{\text{beam},3}} & \frac{\partial \underline{u}_3^{\text{beam},3}}{\partial \underline{\omega}^{\text{beam},3}} \end{bmatrix} \begin{bmatrix} \frac{\partial \underline{u}^{\text{beam},3}}{\partial \underline{z}} \\ \frac{\partial \underline{\omega}^{\text{beam},3}}{\partial \underline{z}} \end{bmatrix} - \\
&\left(\underline{u}_2^{\text{FE},23} - \underline{u}_2^{\text{beam},23}\right)^T \begin{bmatrix} \frac{\partial \underline{u}_2^{\text{beam},23}}{\partial \underline{u}^{\text{beam},23}} & \frac{\partial \underline{u}_2^{\text{beam},23}}{\partial \underline{\omega}^{\text{beam},23}} \end{bmatrix} \begin{bmatrix} \frac{\partial \underline{u}^{\text{beam},23}}{\partial \underline{z}} \\ \frac{\partial \underline{\omega}^{\text{beam},23}}{\partial \underline{z}} \end{bmatrix} - \left(\underline{u}_3^{\text{FE},23} - \underline{u}_3^{\text{beam},23}\right)^T \begin{bmatrix} \frac{\partial \underline{u}_3^{\text{beam},23}}{\partial \underline{u}^{\text{beam},23}} & \frac{\partial \underline{u}_3^{\text{beam},23}}{\partial \underline{\omega}^{\text{beam},23}} \end{bmatrix} \begin{bmatrix} \frac{\partial \underline{u}^{\text{beam},23}}{\partial \underline{z}} \\ \frac{\partial \underline{\omega}^{\text{beam},23}}{\partial \underline{z}} \end{bmatrix},
\end{aligned} \tag{17}$$

where the components of matrices $\frac{\partial \underline{u}_j^{\text{beam},*}}{\partial \underline{u}^{\text{beam},*}}$ (with $*$ denoting e, 2, 3 or 23 and $j = 1, 2, 3$) and $\frac{\partial \underline{\omega}_1^{\text{beam},t}}{\partial \underline{\omega}^{\text{beam},t}}$ equal zero or one. Matrices $\frac{\partial \underline{u}_j^{\text{beam},*}}{\partial \underline{\omega}^{\text{beam},*}}$ and $\frac{\partial \underline{\omega}_1^{\text{beam},t}}{\partial \underline{u}^{\text{beam},t}}$ are zero matrices. The question is how to efficiently compute matrices $\frac{\partial \underline{u}^{\text{beam},*}}{\partial \underline{z}}$ and $\frac{\partial \underline{\omega}^{\text{beam},*}}{\partial \underline{z}}$. To this end, the equilibrium equation in Eq. (12) is again considered, but only after it is solved, and the dependency on parameters $\underline{z}$ is included:

$$\begin{bmatrix} \underline{f}_{\text{int}}(\underline{u}^{\text{beam},*}(\underline{z}), \underline{\omega}^{\text{beam},*}(\underline{z}), \underline{z}) \\ \underline{M}_{\text{int}}(\underline{u}^{\text{beam},*}(\underline{z}), \underline{\omega}^{\text{beam},*}(\underline{z}), \underline{z}) \end{bmatrix} = \begin{bmatrix} \underline{f}_{\text{ext}} \\ \underline{M}_{\text{ext}} \end{bmatrix}. \tag{18}$$

The equilibrium equation is then differentiated with respect to parameters $\underline{z}$:

$$\begin{bmatrix} \frac{\partial \underline{f}_{\text{int}}}{\partial \underline{z}} \\ \frac{\partial \underline{M}_{\text{int}}}{\partial \underline{z}} \end{bmatrix}_{\underline{u}^{\text{beam},*}, \underline{\omega}^{\text{beam},*}} + \begin{bmatrix} \frac{\partial \underline{f}_{\text{int}}}{\partial \underline{u}} & \frac{\partial \underline{f}_{\text{int}}}{\partial \underline{\omega}} \\ \frac{\partial \underline{M}_{\text{int}}}{\partial \underline{u}} & \frac{\partial \underline{M}_{\text{int}}}{\partial \underline{\omega}} \end{bmatrix} \begin{bmatrix} \frac{\partial \underline{u}^{\text{beam},*}}{\partial \underline{z}} \\ \frac{\partial \underline{\omega}^{\text{beam},*}}{\partial \underline{z}} \end{bmatrix} = \begin{bmatrix} \underline{0} \\ \underline{0} \end{bmatrix}, \tag{19}$$

which gives the following expression:

$$\begin{bmatrix} \frac{\partial \underline{u}^{\text{beam},*}}{\partial \underline{z}} \\ \frac{\partial \underline{\omega}^{\text{beam},*}}{\partial \underline{z}} \end{bmatrix} = - \begin{bmatrix} \frac{\partial \underline{f}_{\text{int}}}{\partial \underline{u}} & \frac{\partial \underline{f}_{\text{int}}}{\partial \underline{\omega}} \\ \frac{\partial \underline{M}_{\text{int}}}{\partial \underline{u}} & \frac{\partial \underline{M}_{\text{int}}}{\partial \underline{\omega}} \end{bmatrix}^{-1} \begin{bmatrix} \frac{\partial \underline{f}_{\text{int}}}{\partial \underline{z}} \\ \frac{\partial \underline{M}_{\text{int}}}{\partial \underline{z}} \end{bmatrix}_{\underline{u}^{\text{beam},*}, \underline{\omega}^{\text{beam},*}}. \tag{20}$$

This expression is then incorporated in Eq. (17) and the gradient would be known. However, in that case a problem would remain, which is that the actual inverse of the matrix in Eq. (20) must be computed (i.e. the same matrix as the symmetric stiffness matrix in Eq. (14)), which is rather inefficient. Therefore, instead of only inserting Eq. (20) in Eq. (17), the adjoint of Eq. (17) is taken as well. Since the adjoint is the same as the transpose in case all involved components are real scalars (which is the case here), the resulting expression does not require the actual inverse to be computed as it reads:

$$\begin{aligned}
\frac{\partial J}{\partial \underline{z}} = {} & 2\left[\left(\frac{\partial \underline{f}_{\text{int}}}{\partial \underline{z}}\right)^T \quad \left(\frac{\partial \underline{M}_{\text{int}}}{\partial \underline{z}}\right)^T\right]_{\underline{u}^{\text{beam},e},\underline{\omega}^{\text{beam},e}} \begin{bmatrix} \frac{\partial \underline{f}_{\text{int}}}{\partial \underline{u}} & \frac{\partial \underline{f}_{\text{int}}}{\partial \underline{\omega}} \\ \frac{\partial \underline{M}_{\text{int}}}{\partial \underline{u}} & \frac{\partial \underline{M}_{\text{int}}}{\partial \underline{\omega}} \end{bmatrix}^{-1} \begin{bmatrix} \left(\frac{\partial \underline{u}_1^{\text{beam},e}}{\partial \underline{u}^{\text{beam},e}}\right)^T \\ \left(\frac{\partial \underline{u}_1^{\text{beam},e}}{\partial \underline{\omega}^{\text{beam},e}}\right)^T \end{bmatrix} \left(\underline{u}_1^{\text{FE},e} - \underline{u}_1^{\text{beam},e}\right) + \\
& 2\left[\left(\frac{\partial \underline{f}_{\text{int}}}{\partial \underline{z}}\right)^T \quad \left(\frac{\partial \underline{M}_{\text{int}}}{\partial \underline{z}}\right)^T\right]_{\underline{u}^{\text{beam},t},\underline{\omega}^{\text{beam},t}} \begin{bmatrix} \frac{\partial \underline{f}_{\text{int}}}{\partial \underline{u}} & \frac{\partial \underline{f}_{\text{int}}}{\partial \underline{\omega}} \\ \frac{\partial \underline{M}_{\text{int}}}{\partial \underline{u}} & \frac{\partial \underline{M}_{\text{int}}}{\partial \underline{\omega}} \end{bmatrix}^{-1} \begin{bmatrix} \left(\frac{\partial \underline{\omega}_1^{\text{beam},t}}{\partial \underline{u}^{\text{beam},t}}\right)^T \\ \left(\frac{\partial \underline{\omega}_1^{\text{beam},t}}{\partial \underline{\omega}^{\text{beam},t}}\right)^T \end{bmatrix} \left(\underline{\omega}_1^{\text{FE},t} - \underline{\omega}_1^{\text{beam},t}\right) + \\
& 2\left[\left(\frac{\partial \underline{f}_{\text{int}}}{\partial \underline{z}}\right)^T \quad \left(\frac{\partial \underline{M}_{\text{int}}}{\partial \underline{z}}\right)^T\right]_{\underline{u}^{\text{beam},2},\underline{\omega}^{\text{beam},2}} \begin{bmatrix} \frac{\partial \underline{f}_{\text{int}}}{\partial \underline{u}} & \frac{\partial \underline{f}_{\text{int}}}{\partial \underline{\omega}} \\ \frac{\partial \underline{M}_{\text{int}}}{\partial \underline{u}} & \frac{\partial \underline{M}_{\text{int}}}{\partial \underline{\omega}} \end{bmatrix}^{-1} \begin{bmatrix} \left(\frac{\partial \underline{u}_2^{\text{beam},2}}{\partial \underline{u}^{\text{beam},2}}\right)^T \\ \left(\frac{\partial \underline{u}_2^{\text{beam},2}}{\partial \underline{\omega}^{\text{beam},2}}\right)^T \end{bmatrix} \left(\underline{u}_2^{\text{FE},2} - \underline{u}_2^{\text{beam},2}\right) + \\
& 2\left[\left(\frac{\partial \underline{f}_{\text{int}}}{\partial \underline{z}}\right)^T \quad \left(\frac{\partial \underline{M}_{\text{int}}}{\partial \underline{z}}\right)^T\right]_{\underline{u}^{\text{beam},3},\underline{\omega}^{\text{beam},3}} \begin{bmatrix} \frac{\partial \underline{f}_{\text{int}}}{\partial \underline{u}} & \frac{\partial \underline{f}_{\text{int}}}{\partial \underline{\omega}} \\ \frac{\partial \underline{M}_{\text{int}}}{\partial \underline{u}} & \frac{\partial \underline{M}_{\text{int}}}{\partial \underline{\omega}} \end{bmatrix}^{-1} \begin{bmatrix} \left(\frac{\partial \underline{u}_3^{\text{beam},3}}{\partial \underline{u}^{\text{beam},3}}\right)^T \\ \left(\frac{\partial \underline{u}_3^{\text{beam},3}}{\partial \underline{\omega}^{\text{beam},3}}\right)^T \end{bmatrix} \left(\underline{u}_3^{\text{FE},3} - \underline{u}_3^{\text{beam},3}\right) + \\
& \left[\left(\frac{\partial \underline{f}_{\text{int}}}{\partial \underline{z}}\right)^T \quad \left(\frac{\partial \underline{M}_{\text{int}}}{\partial \underline{z}}\right)^T\right]_{\underline{u}^{\text{beam},23},\underline{\omega}^{\text{beam},23}} \begin{bmatrix} \frac{\partial \underline{f}_{\text{int}}}{\partial \underline{u}} & \frac{\partial \underline{f}_{\text{int}}}{\partial \underline{\omega}} \\ \frac{\partial \underline{M}_{\text{int}}}{\partial \underline{u}} & \frac{\partial \underline{M}_{\text{int}}}{\partial \underline{\omega}} \end{bmatrix}^{-1} \begin{bmatrix} \left(\frac{\partial \underline{u}_2^{\text{beam},23}}{\partial \underline{u}^{\text{beam},23}}\right)^T \\ \left(\frac{\partial \underline{u}_2^{\text{beam},23}}{\partial \underline{\omega}^{\text{beam},23}}\right)^T \end{bmatrix} \left(\underline{u}_2^{\text{FE},23} - \underline{u}_2^{\text{beam},23}\right) + \\
& \left[\left(\frac{\partial \underline{f}_{\text{int}}}{\partial \underline{z}}\right)^T \quad \left(\frac{\partial \underline{M}_{\text{int}}}{\partial \underline{z}}\right)^T\right]_{\underline{u}^{\text{beam},23},\underline{\omega}^{\text{beam},23}} \begin{bmatrix} \frac{\partial \underline{f}_{\text{int}}}{\partial \underline{u}} & \frac{\partial \underline{f}_{\text{int}}}{\partial \underline{\omega}} \\ \frac{\partial \underline{M}_{\text{int}}}{\partial \underline{u}} & \frac{\partial \underline{M}_{\text{int}}}{\partial \underline{\omega}} \end{bmatrix}^{-1} \begin{bmatrix} \left(\frac{\partial \underline{u}_3^{\text{beam},23}}{\partial \underline{u}^{\text{beam},23}}\right)^T \\ \left(\frac{\partial \underline{u}_3^{\text{beam},23}}{\partial \underline{\omega}^{\text{beam},23}}\right)^T \end{bmatrix} \left(\underline{u}_3^{\text{FE},23} - \underline{u}_3^{\text{beam},23}\right). \qquad (21)
\end{aligned}$$

4. Formulations of the random fields

In this section we discuss the methodologies used to construct the (intercorrelated) random fields with bounds. Thus, we first briefly discuss GPs, then the copula theorem, then the concept of Gaussian copula process, and finally the different frameworks to formulate multi-output fields. Note that random fields are stochastic processes with spatial variables as their index (input) set. To avoid confusion, the term *process* is used to discuss the main concepts.

4.1. Gaussian processes

The GP is one of the main components of the frameworks employed in this contribution to formulate multi-output random fields. This subsection aims to present GPs in a practical way. Readers interested in more details are referred to [7].

A GP is an extension of a multivariate Gaussian distribution to an infinite-dimensional Gaussian distribution [9]. Any finite-dimensional marginal distribution of a GP is still Gaussian. A GP is characterized by its mean $m(x_1)$ and covariance function $k(x_1, x_1')$, where x_1 and x_1' denote two axial locations (which may be the same). A realization of a Gaussian process can be written as follows:

$$w(x_1) \sim \text{GP}(m(x_1), k(x_1, x_1')). \qquad (22)$$

The values of w at any n given points are drawn (realizations) from an n-dimensional Gaussian distribution with mean $\underline{m} = \begin{bmatrix} m({x_1}^1) & \cdots & m({x_1}^n) \end{bmatrix}^T$ and covariance matrix $\underline{\underline{K}}$ with $(K)_{ij} = k(x_1^i, x_1^j)$ or $w({x_1}^1), \cdots, w({x_1}^n) \sim N(\underline{m}, \underline{\underline{K}})$. Frequent choices for the covariance function can be found in [7] and [10]. Often furthermore (as in this contribution), $m(x_1) = 0$.

4.2. Copulas

As mentioned before, conventional Gaussian processes do not incorporate bounds and are therefore (at least theoretically) not able to incorporate the bounds of physical parameters. The framework given in [6] discusses how to separate the correlation structure of a GP from its marginal univariate distributions (i.e. Gaussian distribution) using the copula theorem [17]. This enables replacing the univariate marginal Gaussian distribution in a GP with another (e.g. bounded) distribution. This subsection briefly discusses the copula theorem. More details can be found in [17].

A copula is a function that models the dependency between several random variables *regardless* of their univariate marginal distributions. In practice a copula takes the cumulative distribution function (CDF) of each random variable and joins them to create the corresponding multivariate joint CDF. Once the joint CDF is formulated, the joint PDF can be derived.

Let $\underline{P} = \begin{bmatrix} P_1 & \cdots & P_{n_p} \end{bmatrix}^T$ denote a set of n_p random variables ($n_p = 2000$ here), Π denotes the joint CDF of the random variables and Π_i denotes the marginal univariate CDF of each random variable. Based on Sklar's theorem [64], an n_p-dimensional copula, C, exists such that:

$$\Pi(p_1, \cdots, p_{n_p}) = C(\Pi_1(p_1), \cdots, \Pi_{n_p}(p_{n_p})), \tag{23}$$

with its associated joint PDF reading as:

$$\pi(p_1, \cdots, p_{n_p}) = c(\Pi_1(p_1), \cdots, \Pi_{n_p}(p_{n_p})) \prod_{i=1}^{n_p} \pi_i(p_i), \tag{24}$$

where $c(v_1, \cdots, v_{n_p}) = \frac{\partial C(v_1, \cdots, v_{n_p})}{\partial v_1 \cdots \partial v_{n_p}}$ with $v_i = \Pi_i(p_i)$ and $\pi_i(p_i)$ denotes the i^{th} marginal PDF.

A multivariate Gaussian distribution can be considered a set of univariate Gaussian distributions that are joined by a Gaussian copula. Let $v_i = \Pi_i(p_i)$, $\underline{\underline{\Gamma}}_C \in [-1, 1]^{n_p \times n_p}$ denote a Pearson correlation matrix (Pearson's ρ is a measure for the linear relationship between two random variables, see e.g. [65]), $\Phi(\tilde{p})$ denote the standard Gaussian CDF (i.e. $\tilde{p} \sim N(0,1) = \frac{1}{\sqrt{2\pi}} \exp(-\frac{\tilde{p}^2}{2})$), $|\cdot|$ denote the determinant and $\underline{\underline{I}}$ the $n_p \times n_p$ identity matrix. The density of a Gaussian copula can then be expressed as [18]:

$$c(\underline{v}|\underline{\underline{\Gamma}}_C) = \frac{1}{\sqrt{|\underline{\underline{\Gamma}}_C|}} \exp\Big(-\frac{1}{2} \begin{bmatrix} \Phi^{-1}(v_1) & \cdots & \Phi^{-1}(v_{n_p}) \end{bmatrix} \times (\underline{\underline{\Gamma}}_C^{-1} - \underline{\underline{I}}) \times \begin{bmatrix} \Phi^{-1}(v_1) & \cdots & \Phi^{-1}(v_{n_p}) \end{bmatrix}^T \Big). \tag{25}$$

4.3. Combining Gaussian processes with the copula theorem

As mentioned in Subsection 4.1, a GP is generalization of a multivariate Gaussian distribution. This entails that the copula theorem given in Subsection 4.2 can be used to write any finite-dimensional marginal distribution of a Gaussian process as a multiplication of univariate Gaussian distributions and the Gaussian copula of Eq. (24). Consequently, the univariate marginal Gaussian distribution of a GP can be changed to any other distribution, whilst the GP's correlation structure (here spatial) remains unchanged. The joint PDF for an n_p-dimensional marginalization of the desired process will be in the form of Eq. (24) where the univariate Gaussian distribution is replaced by another distribution.

A sample of such a process can in practice be generated as follows:

(1) draw a sample from a GP with a given covariance function,

(2) use the standard univariate Gaussian CDF to transform each scalar of the sample drawn in step (1) to a scalar drawn from a uniform distribution, and

(3) transform the scalars through the inverse CDF of the distribution of choice.

4.4. Multi-output random process

So far, this section has focused on a single process (including the spatial correlation). However, the main idea of this contribution is to combine several (five) fields/processes, which come with additional correlations: the correlations between the individual processes. In this subsection, formulations are discussed that combine the aforementioned concepts in order to create multi-output processes/fields with mutual correlations. The formulations presented in this subsection are special cases of a more general methodology known as the linear model of coregionalization (LMC, see [34]) where the processes are modeled as a linear combination of independent random functions. The LMC

guarantees that the covariance function of the final, multi-output process is a valid positive semidefinite function. Once the covariance function is expressed (and consequently, the covariance matrix for finite-dimensional case), the copula theorem is employed to transform the Gaussian process to a random process with the desired univariate marginal distributions and the Gaussian correlation structure.

4.4.1. Intrinsic coregionalization model (ICM)

As mentioned before, the multi-output process are modeled as a linear combination of single random processes. In the intrinsic coregionalization model (ICM) each field is expressed by linearly combining realizations from a single latent GP. For simplicity, ICM is discussed below for the case of two fields.

Let $w^1(x_1)$ and $w^2(x_1)$ denote the two outputs and $\delta(x_1) \sim \mathrm{GP}(0, k_\delta(x_1, x_1'))$. The output of the ICM can then be written as:

$$\begin{aligned} w_1(x_1) &= a^{11}\delta^1(x_1) + a^{12}\delta^2(x_1) \\ w_2(x_1) &= a^{21}\delta^1(x_1) + a^{22}\delta^2(x_1) \end{aligned}, \tag{26}$$

where $\delta^1(x_1)$ and $\delta^2(x_1)$ denote two realizations from $\delta(x_1) \sim \mathrm{GP}(0, k_\delta(x_1, x_1'))$. Eq. (26) can be rewritten as:

$$\underline{w}(x_1) = \underline{\underline{A}}\,\underline{\delta}(x_1), \tag{27}$$

with:

$$\underline{\underline{A}} = \begin{bmatrix} \underline{a}^1 & \underline{a}^2 \end{bmatrix} = \begin{bmatrix} a^{11} & a^{12} \\ a^{21} & a^{22} \end{bmatrix} \qquad \underline{\delta}(x_1) = \begin{bmatrix} \delta^1(x_1) \\ \delta^2(x_1) \end{bmatrix}. \tag{28}$$

Consequently, the resulting covariance function reads as [34]:

$$\mathrm{cov}(\underline{w}(x_1), \underline{w}(x_1')) = \underline{\underline{B}} k_\delta(x_1, x_1'), \tag{29}$$

with $\underline{\underline{B}} = \underline{\underline{A}}\,\underline{\underline{A}}^T$. The covariance matrix corresponding to the input column $\underline{x} = \begin{bmatrix} x_1^1 & \cdots & x_1^{n_i} \end{bmatrix}^T$ equals to:

$$\underline{\underline{K}} = \underline{\underline{B}} \otimes \underline{\underline{K}}_\delta, \tag{30}$$

where $(\underline{\underline{K}}_\delta)_{ij} = k_\delta(x_1^i, x_1^j)$ and $\otimes$ denotes the Kronecker product. Consequently, the distribution for the two process case reads:

$$\begin{bmatrix} \underline{w}^1 \\ \underline{w}^2 \end{bmatrix} \sim N\left(\begin{bmatrix} \underline{0} \\ \underline{0} \end{bmatrix}, \begin{bmatrix} (B)_{11}\underline{\underline{K}}_\delta & (B)_{12}\underline{\underline{K}}_\delta \\ (B)_{21}\underline{\underline{K}}_\delta & (B)_{22}\underline{\underline{K}}_\delta \end{bmatrix} \right). \tag{31}$$

In the general case of an n_d-dimensional output system with n_r realizations from $\delta(x_1)$ we have:

$$w^i(x_1) = \sum_{j=1}^{n_r} a^{ij}\delta^j(x_1), \tag{32}$$

where $i = 1, \cdots, n_d$, n_r denotes the number of samples and $\delta^j(x_1)$ denotes a single realization, independently sampled from $\delta(x_1) \sim (0, k_\delta(x_1, x_1'))$. Once again, the resulting covariance function is given by Eq. (29), where $\underline{\underline{B}} = \underline{\underline{A}}\,\underline{\underline{A}}^T$, $\underline{\underline{A}} = \begin{bmatrix} \underline{a}^1 \cdots \underline{a}^{n_r} \end{bmatrix}$ and $\underline{a}^j = \begin{bmatrix} \underline{a}^{1j} \cdots \underline{a}^{n_d j} \end{bmatrix}^T$. For a finite set of n_i inputs the corresponding covariance matrix is given by Eq. (30). Note that $\underline{\underline{B}}$ is a $n_d \times n_d$ symmetric and positive semi-definite matrix.

4.4.2. Semiparametric latent factor model (SLFM)

Various studies [27, 28, 30, 32, 33] have used the ICM formulation because of its relatively simple parameterization and reduced complexity compared to the LMC. However, the ICM formulation can be restrictive as it uses only one latent GP and assumes that all the outputs share the same spatial dependency/correlation structure. In this subsection we briefly discuss the SLFM formulation, which is (similar to the ICM formulation) a simplified version of the LMC, but includes more than only one latent GP.

The SLFM formulation uses n_r realizations from n_r latent GPs. Similar to the previous subsection, the two-output scenario is considered (i.e. $\underline{w} = \begin{bmatrix} w^1(x_1) & w^2(x_1) \end{bmatrix}^T$) with $\delta^1(x_1) \sim \mathrm{GP}(0, k_{\delta^1}(x_1, x_1'))$ and $\delta^2(x_1) \sim \mathrm{GP}(0, k_{\delta^2}(x_1, x_1'))$. Similar to the ICM, the output is a linear combination of realizations $\delta^1(x_1)$ and $\delta^2(x_1)$ (see Eqs. (26) and (27)).

Note that $\delta^1(x_1)$ and $\delta^2(x_1)$ are realizations from different GPs while in the ICM they are realizations from the same GP. Consequently, the resulting covariance function reads [34]:

$$\text{cov}(\underline{w}(x_1), \underline{w}(x_1')) = \underline{\underline{B}}^1 k_{\delta^1}(x_1, x_1') + \underline{\underline{B}}^2 k_{\delta^2}(x_1, x_1'), \tag{33}$$

where $\underline{\underline{B}}^1 = \underline{a}^1(\underline{a}^1)^T$ and $\underline{\underline{B}}^2 = \underline{a}^2(\underline{a}^2)^T$. Furthermore, the covariance matrix corresponding to input $\underline{x}_1 = \begin{bmatrix} x_1^1 & \cdots & x_1^{n_i} \end{bmatrix}^T$ reads:

$$\underline{\underline{K}} = \underline{\underline{B}}^1 \otimes \underline{\underline{K}}_{\delta^1} + \underline{\underline{B}}^2 \otimes \underline{\underline{K}}_{\delta^2}, \tag{34}$$

with $(\underline{\underline{K}}_{\delta^1})_{ij} = k_{\delta^1}(x_1^i, x_1^j)$ and $(\underline{\underline{K}}_{\delta^2})_{ij} = k_{\delta^2}(x_1^i, x_1^j)$. Considering the more general case of n_d outputs, the covariance function can be written as:

$$\text{cov}(\underline{w}(x_1), \underline{w}(x_1')) = \sum_{j=1}^{n_r} \underline{a}^j (\underline{a}^j)^T k_{\delta^j}(x_1, x_1') = \sum_{j=1}^{n_r} \underline{\underline{B}}^j k_{\delta^j}(x_1, x_1') \tag{35}$$

where $\underline{a}^j = \begin{bmatrix} \underline{a}^{1j} \cdots \underline{a}^{n_d j} \end{bmatrix}^T$. Furthermore, the covariance matrix reads:

$$\underline{\underline{K}} = \sum_{j=1}^{n_r} \underline{\underline{B}}^j \otimes \underline{\underline{K}}_{\delta^j}. \tag{36}$$

5. Bayesian inference

Let $\underline{z}$ be the set of n_o observations and $\underline{p}$ the set of n_p parameters to be identified. Bayes' theorem can then be expressed as:

$$\pi(\underline{p}|\underline{z}) = \frac{\pi(\underline{p})\pi(\underline{z}|\underline{p})}{\pi(\underline{z})} = \frac{1}{\zeta}\pi(\underline{p})\pi(\underline{z}|\underline{p}), \tag{37}$$

where $\pi(\underline{p})$ denotes the prior PDF (describing the user's a-priori knowledge about the parameters; e.g. some parameters cannot be negative), $\pi(\underline{z}|\underline{p})$ denotes the likelihood function (quantifying the plausibility of an observation set, for a given set of parameters), $\pi(\underline{p}|\underline{z})$ denotes the posterior PDF (quantifying the plausibility of a parameter set, for a given set of observations) and $\pi(\underline{z})$ is called the evidence. The value of the evidence is known after the observations are made. For this reason, it equals a constant number ($\pi(\underline{z}) = \zeta \in \mathbb{R}^+$). Equivalently, we can omit normalization constant ζ and write the unnormalized posterior density as:

$$\pi(\underline{p}|\underline{z}) \propto \pi(\underline{p})\pi(\underline{z}|\underline{p}). \tag{38}$$

Often the posterior has a complex shape and as a result calculating the statistical summaries of the posterior, such as the mean, the MAP (i.e. the 'maximum-a-posteriori-probability': the parameter values at which the posterior is maximal) and the covariance matrix (i.e. the matrix that measures the correlation between the parameters) must be obtained using sampling approaches such as Markov chain Monte Carlo (MCMC) techniques [66]. Readers are referred to [46, 67] for more details.

6. Sequence and details of the identification

The neatest identification framework would consider all the random fields' parameters in a single framework that considers the results of the FE simulations as measurements and the beam simulation as forward model (i.e. the model that defines likelihood function). The first problem with such an approach is that a substantial number of random variables is present (i.e. the random fields' parameters), which makes the approximation of the posterior, and in particular the tuning of the sampling parameters, computationally inefficient. The second problem is that the beam simulation must be repeated numerous of times per sampling point, hereby adding even more time to the posterior sampling. Section 2 has already made clear that the identification is split in a part in which realizations of the random fields are deterministically identified per strut and a part in which the random fields' parameters are probabilistically identified. On top of that, the probabilistic part of the identification itself is also split in different steps. This section discusses these steps in chronological order and presents the required details of each step.

In order to reduce the number of the random variables per step as well as avoiding issues with system identifiability, the parameters of the univariate marginal PDF of each field (i.e. the fields are the fields of r_a, r_b, r_c, r_o and ν) are identified first. The MAP estimates of the univariate marginal PDFs' parameters are then considered to be true values and are kept constant in the subsequent steps. This simplification is reasonable as the number of observations for the univariate marginal PDFs is considerably large. Furthermore, it is assumed that the field of Poisson's ratio is independent of the fields of the geometrical parameters.

6.1. Deterministic identification of six struts

Sections 2 and 3 have already made clear that a conjugate gradient approach is employed to deterministically identify the beam elements' parameters ($\underline{z} = \begin{bmatrix}\underline{z}_{r_a}^T & \underline{z}_{r_b}^T & \underline{z}_{r_c}^T & \underline{z}_{r_o}^T & \underline{z}_{\nu}^T\end{bmatrix}^T$) for each strut. In the subsequent probabilistic identification, these parameters are considered as observations and the parameters to be identified are the random fields' parameters.

The objective function to be minimized in the deterministic identification was yet presented in Eq. (15), whilst the objective function's gradient is computationally efficiently evaluated using Eq (21). Some details that are not yet mentioned are that the conjugate gradient direction is taken as proposed by [68], which is reset after every 50 iterations. A backtracking line search is furthermore employed with the Armijo rule and without curvature condition. The exact conjugate direction is taken as the initial step size, which is reduced with a factor of 50% every time the step size does not abide the Armijo rule. The slope of the Armijo rule is given by the inner product of the conjugate gradient direction and steepest descent direction, multiplied with a factor of 0.5.

6.2. Univariate marginal PDFs

6.2.1. Poisson's ratio

Although for the beam model, the typical upper bound of Poisson's ratio is not strictly required, both the traditional lower bound and upper bound are incorporated (i.e. $-1 < \nu < 0.5$). To this end, a four parameter beta distribution is chosen as the univariate marginal PDF:

$$\pi_\nu(\nu) = \frac{(\nu - c_{\nu_1})^{\alpha_\nu - 1}(c_{\nu_2} - \nu)^{\beta_\nu - 1}}{(c_{\nu_2} - c_{\nu_1})^{\alpha_\nu + \beta_\nu - 1} B(\alpha_\nu, \beta_\nu)}, \tag{39}$$

where $c_{\nu_1} = -1$ and $c_{\nu_2} = 0.5$ denote the known lower and upper bounds, respectively, and α_ν and β_ν denote the parameters governing the shape of the PDF. $B(\cdot,\cdot)$ denotes the beta function. Thus, the parameters to be identified here are $\underline{p}_\nu = \begin{bmatrix}\alpha_\nu & \beta_\nu\end{bmatrix}^T$. Assuming $\underline{z}_\nu$ denotes a column with $n_\nu = 2400$ observations (400 Poisson's ratios per strut), the Bayesian formula can be rewritten as:

$$\pi(\alpha_\nu, \beta_\nu | \underline{z}_\nu) \propto \pi(\alpha_\nu)\pi(\beta_\nu) \prod_{i=1}^{n_\nu} \pi((z_\nu)_i | \alpha_\nu, \beta_\nu), \tag{40}$$

where $\pi(\alpha_\nu)$ and $\pi(\beta_\nu)$ together form the uncorrelated prior and $\pi((z_\nu)_i|\alpha_\nu, \beta_\nu)$ denotes the likelihood in Eq. (39). Once the posterior distribution is formulated, the Metropolis algorithm with an adaptive proposal distribution [69] is used to approximate the posterior and to obtain its MAP estimates.

6.2.2. Geometrical parameters

Since the geometrical parameters (i.e. r_a, r_b, r_c and r_o) are distances, their values cannot be negative. This is one of the reasons that the Weibull distribution is employed for all of these fields. Another reason is that the Weibull distribution can model left-skewed observations (empirical skewness of r_a and r_b show that they are left-skewed). The Weibull distribution reads:

$$\pi_{p_i}(p_i) = \frac{\alpha_{p_i}}{\theta p_i}\Big(\frac{p_i}{\theta_{p_i}}\Big)^{\alpha_{p_i}-1} \exp\Big(-\frac{p_i}{\theta_{p_i}}\Big)^{\alpha_{p_i}} \quad p_i \geq 0, \tag{41}$$

where p_i denotes each of the geometrical parameters. Furthermore, $\alpha_{p_i} > 0$ denotes the shape parameter and $\theta_{p_i} > 0$ denotes the scale parameter of the Weibull distribution. The parameters to be identified for the univariate marginal PDF of each geometrical parameter are $\underline{p}_{p_i} = \begin{bmatrix}\alpha_{p_i} & \theta_{p_i}\end{bmatrix}^T$. Similar to the case of Poisson's ratio, for $n_{p_i} = 2400$ observations the Bayesian formulation reads:

$$\pi(\alpha_{p_i}, \theta p_i | \underline{z}_{p_i}) \propto \pi(\alpha_{p_i})\pi(\theta_{p_i}) \prod_{j=1}^{n_{p_i}} \pi((z_{p_i})_j | \alpha_{p_i}, \theta_{p_i}), \tag{42}$$

where $\pi(\alpha_{p_i})$ and $\pi(\theta_{p_i})$ again denote our priors and $\pi((z_{p_i})_i|\alpha_{p_i},\theta_{p_i})$ denotes the likelihood in Eq. (41).

6.3. Random fields' parameters, given the univariate marginal PDFs

As mentioned before, once the MAP estimates for the univariate marginal PDFs' parameters are obtained, they are treated as constants for the identification of the remaining parameters of the random fields.

To model the random fields, three cases are considered:

(1) all the parameter fields are independent,

(2) the field of Poisson's ratio is independent and the fields of the geometrical parameters are modeled using the ICM method of Subsection 4.4.1, and

(3) the Poisson's ratio field is independent and the fields of the structure parameters are modeled by the SLFM method of Subsection 4.4.2.

Since in each case the field of Poisson's ratio is modeled independently, it is considered first.

6.3.1. Poisson's ratio

Let $n_r = 6$ denote the number of struts selected for identification and $n_i = 100$[2] denote the number of observations per strut (at $n_i = 100$ different axial locations). Furthermore, let $c_{\nu_1} = -1$, $c_{\nu_2} = 0.5$, α_ν^{MAP} and β_ν^{MAP} denote the known parameters of the univariate marginal PDF (see Eq. (39)). The frequently employed squared exponential covariance function (Eq. (43)) is used to model the spatial correlation between the observations.

$$k_\nu(x_1, x_1') = \exp\big(-\frac{(x_1 - x_1')^2}{2\psi_\nu^2}\big), \tag{43}$$

where ψ_ν denotes the length scale parameter that controls the smoothness of the random field. It is important to note that a covariance function must be selected so that the identified parameters converge if the number of observations per strut increases (i.e. as the spatial mesh gets refined in the fixed domain of strut).

The only parameter to be identified here is ψ_ν. Rewriting the Bayesian formula for a single strut (i.e. the r^{th}) strut, yields:

$$\pi(\psi_\nu|\underline{z}_\nu^r) \propto \pi(\underline{z}_\nu^r|\psi_\nu)\pi(\psi_\nu), \tag{44}$$

where $\underline{z}_\nu^r$ denotes the column of Poisson's ratios per strut. The likelihood $\pi(\underline{z}_\nu^r|\psi_\nu)$ reads as:

$$\pi(\underline{z}_\nu^r|\psi_\nu) = c(\underline{v}_{\underline{z}_\nu^r}|\underline{\underline{\Gamma}}_{C_\nu}) \prod_{i=1}^{n_i} \pi_\nu((\underline{z}_\nu^r)_i), \tag{45}$$

where $\pi_\nu(\cdot)$ is given in Eq. (39), $(\underline{v}_{\underline{z}_\nu^r})_i$ denotes the value of the four parameter beta CDF at $(\underline{z}_\nu^r)_i$, $c(\cdot|\cdot)$ is given in Eq. (25) and $(\underline{\underline{\Gamma}}_{C_\nu})_{lm} = \exp\big(-\frac{((x_1)_l-(x_1)_m)^2}{2\psi_\nu^2}\big)$. Furthermore, $n_i = 100$ denotes the number of Poisson's ratios per strut, identified with the deterministic identification approach per strut. Finally, the likelihood function for all $n_r = 6$ struts reads:

$$\pi(\underline{z}_\nu|\psi_\nu) = \prod_{r=1}^{n_r} c(\underline{v}_{\underline{z}_\nu^r}|\underline{\underline{\Gamma}}_{C_\nu}) \prod_{i=1}^{n_i} \pi_\nu((\underline{z}_\nu^r)_i), \tag{46}$$

and the posterior reads:

$$\pi(\psi_\nu|\underline{z}_\nu) \propto \pi(\underline{z}_\nu|\psi_\nu)\pi(\psi_\nu), \tag{47}$$

where $\underline{z}_\nu$ collects the Poisson's ratios of all six struts identified with the deterministic identification.

[2]To avoid numerical instabilities due to the observations that are positioned very close to each other we select 100 observations out of the 400 observations for each strut.

6.3.2. Geometrical parameters

(A) Independent fields. Arguably the most straightforward approach is to describe each random field completely independently (i.e. without mutual correlation). This will serve as the reference case and and only requires the length scale parameter of each field to be independent (on top of the parameters of the univariate marginal PDF of each field). The identification of completely independent random fields is thus effectively the same as described for Poisson's ratio in the previous subsection 6.3.1, except that the univariate marginal PDF is the Weibull distribution and that a Matérn class [7] covariance function is employed to describe spatial correlation.

Let $\alpha_{p_i}^{\text{MAP}}$ and $\theta_{p_i}^{\text{MAP}}$ denote the MAP estimates for the parameters of the Weibull distribution of each field that is not the field of Poisson's ratio (i.e. p_i can be r_a, r_b, r_c or r_o). The Matérn covariance function which asymptotically converges for an increase of the number of locations increases reads:

$$k_{p_i} = \Big(1 + \frac{\sqrt{3}|x_1 - x_1'|}{\psi_{p_i}}\Big)\exp\Big(-\frac{\sqrt{3}|x_1, -x_1'|}{\psi_{p_i}}\Big) \tag{48}$$

where the length scale parameter to be identified is denoted by ψ_{p_i}. Similar to the case of Poisson's ratio for $n_r = 6$ struts, the posterior is expressed as follows:

$$\pi(\psi_{p_i}|\underline{z}_{p_i}) \propto \pi(\underline{z}_{p_i}|\psi_{p_i})\pi(\psi_{p_i}), \tag{49}$$

and

$$\pi(\underline{z}_{p_i}|\psi_{p_i}) = \prod_{r=1}^{n_r} c(\underline{v}_{\underline{z}_{p_i}^r}|\underline{\underline{\Gamma}}_{C_{p_i}}) \prod_{j=1}^{n_i} \pi_{p_i}((\underline{z}_{p_i}^r)_j), \tag{50}$$

where $\underline{z}_{p_i}$ denotes the column with all geometrical parameters p_i identified with the deterministic identification. Column $\underline{z}_{p_i}^r$ collects these geometrical parameters for each r^{th} strut (i.e. $\underline{z}_{p_i}^r$ is effectively a subset of $\underline{z}_{p_i}$), $\pi_{p_i}(\cdot)$ is given in Eq. (41) $(\underline{v}_{\underline{z}_{p_i}^r})_j$ denotes the value of the CDF for the Weibull distribution at $(\underline{z}_{p_i}^r)_j$, $c(\cdot|\cdot)$ is given in Eq. (25) and $(\underline{\underline{\Gamma}}_{C_{p_i}})_{lm} = \Big(1 + \frac{\sqrt{3}|(x_1)_l - (x_1)_m|}{\psi_{p_i}}\Big)\exp\Big(-\frac{\sqrt{3}|(x_1)_l - (x_1)_m|}{\psi_{p_i}}\Big)$.

(B) ICM. Unlike in the case of independent fields, the random fields of each geometrical parameter (p_i) are correlated to each other, using only one (latent) GP. The ICM's correlation structure is given in product form of a matrix that defines the correlation between the geometrical parameters and a covariance function which describes the spatial correlation (see Eqs. (29) and (30)). Assuming that the field of each geometrical parameter is described by a linear combination of four realizations from a single latent GP, matrices $\underline{\underline{B}}$, $\underline{\underline{K}}_\delta$ and $\underline{\underline{K}}$ are given by Eqs. (30) and (51). The covariance function of the latent GP is chosen as a Matérn covariance function, which reads:

$$k_\delta = \Big(1 + \frac{\sqrt{3}|x_1 - x_1'|}{\psi_\delta}\Big)\exp\Big(-\frac{\sqrt{3}|x_1 - x_1'|}{\psi_\delta}\Big). \tag{51}$$

Furthermore, matrix $\underline{\underline{B}}$ is a symmetric 4×4 matrix with ten parameters to be identified. Together with a single length scale parameter, ψ_δ, this entails that the number of parameters to be identified is 11. However, an important characteristic of the Gaussian copula is that it uses the correlation matrix to model the dependency structure of the observations. Combining this characteristic with the fact that the Kronecker product of two correlation matrices (see Eq. (30)) equals the correlation matrix of the Kronecker product of the corresponding covariance matrices [70], the number of parameters can be reduced to seven. Note that all diagonal components of a correlation matrix equal one and therefore do not need to be identified. Bayes' theorem per strut can be expressed as follows:

$$\pi(\underline{\gamma}_{\underline{\underline{B}}}, \psi_\delta|\underline{z}^r \propto \pi(\underline{z}^r|\underline{\gamma}_{\underline{\underline{B}}}, \psi_\delta)\pi(\underline{\gamma}_{\underline{\underline{B}}})\pi(\psi_\delta), \tag{52}$$

where $\underline{z}^r = \begin{bmatrix}(\underline{z}_{r_a}^r)^T & (\underline{z}_{r_b}^r)^T & (\underline{z}_{r_c}^r)^T & (\underline{z}_{r_o}^r)^T\end{bmatrix}^T$ denotes the column with all the geometrical parameters of the r^{th} strut, $\underline{\gamma}_{\underline{\underline{B}}}$ denotes the column with the non-diagonal components of the correlation matrix for $\underline{\underline{B}}$ (i.e. $\underline{\underline{\Gamma}}_{\underline{\underline{B}}}$) and:

$$\pi(\underline{z}^r|\underline{\gamma}_{\underline{\underline{B}}}, \psi_\delta) = c(\begin{bmatrix}\underline{v}_{\underline{z}_{r_a}^r} \underline{v}_{\underline{z}_{r_b}^r} \underline{v}_{\underline{z}_{r_c}^r} \underline{v}_{\underline{z}_{r_o}^r}\end{bmatrix}^T |\underline{\underline{\Gamma}}_{C_{\text{ICM}}}) \prod_{i=1}^{n_i} \pi_{r_a}((\underline{z}_{r_a}^r)_i)\pi_{r_b}((\underline{z}_{r_b}^r)_i)\pi_{r_c}((\underline{z}_{r_c}^r)_i)\pi_{r_o}((\underline{z}_{r_o}^r)_i), \tag{53}$$

where $\pi_{r_a}(\cdot)$, $\pi_{r_b}(\cdot)$, $\pi_{r_c}(\cdot)$ and $\pi_{r_o}(\cdot)$ are given in Eq. (41), $(\underline{v}_{\underline{z}_{r_a}^r})_i$, $(\underline{v}_{\underline{z}_{r_b}^r})_i$, $(\underline{v}_{\underline{z}_{r_c}^r})_i$ and $(\underline{v}_{\underline{z}_{r_o}^r})_i$ denote the values of the CDF for corresponding Weibull distributions at $(\underline{z}_{r_a}^r)_i$, $(\underline{z}_{r_b}^r)_i$, $(\underline{z}_{r_c}^r)_i$ and $(\underline{z}_{r_o}^r)_i$, $c(\cdot|\cdot)$ is given in Eq. (25),

$\underline{\underline{\Gamma}}_{C_{\text{ICM}}} = \underline{\underline{\Gamma}}_{\underline{\underline{B}}} \otimes \underline{\underline{K}}_{\delta}$ with $(\underline{\underline{K}}_{\delta})_{lm} = \Big(1 + \frac{\sqrt{3}|(x_1)_l - (x_1)_m|}{\psi_\delta}\Big)\exp\Big(-\frac{\sqrt{3}|(x_1)_l - (x_1)_m|}{\psi_\delta}\Big)$. Finally, the posterior for all $n_r = 6$ struts can be written as:

$$\pi(\underline{\gamma}_{\underline{\underline{B}}}, \psi_\delta|\underline{z}) \propto \prod_{r=1}^{n_r} c(\Big[\underline{v}_{\underline{z}^r_{r_a}}\ \underline{v}_{\underline{z}^r_{r_b}}\ \underline{v}_{\underline{z}^r_{r_c}}\ \underline{v}_{\underline{z}^r_{r_o}}\Big]^T |\underline{\underline{\Gamma}}_{C_{\text{ICM}}}) \prod_{i=1}^{n_i} \pi_{r_a}((\underline{z}^r_{r_a})_i)\pi_{r_b}((\underline{z}^r_{r_b})_i)\pi_{r_c}((\underline{z}^r_{r_c})_i)\pi_{r_o}((\underline{z}^r_{r_o})_i)\pi(\underline{\gamma}_{\underline{\underline{B}}})\pi(\psi_\delta). \quad (54)$$

(C) SLFM. The parameterization of the ICM formulation is relatively simple which makes its identification rather traceable. If the multiple outputs depend on the same input set and are of similar type the assumption of similar spatial correlation structure between the outputs used in the ICM serves well [27]. However, if the correlation between the outputs is weak they can have different length scales and [27] proposes to model the fields independently.

Alternatively in this contribution we model the outputs as four independent random fields linearly combined with a shared latent GP. The shared latent GP models the correlation between the outputs. This is equivalent to an SFLM formulation with five latent GPs where $\underline{a}^1 = \begin{bmatrix}1 & 0 & 0 & 0\end{bmatrix}^T$, $\underline{a}^2 = \begin{bmatrix}0 & 1 & 0 & 0\end{bmatrix}^T$, $\underline{a}^3 = \begin{bmatrix}0 & 0 & 1 & 0\end{bmatrix}^T$, $\underline{a}^4 = \begin{bmatrix}0 & 0 & 0 & 1\end{bmatrix}^T$ and the vector $\underline{a}^5$ which defines matrix $\underline{\underline{B}}^5$ in Eqs. (35) and (36) that is to be identified. Similar to previous cases we choose the Matérn class covariance function in Eq. (48) for the outputs where p_i can be r_a, r_b, r_c or r_o. We also choose the same form of covariance function for the shared latent GP with ψ_{shared} as its defining parameter. In total we need to identify nine parameters which are $\underline{a}^5 = \begin{bmatrix}a^5_1 & a^5_2 & a^5_3 & a^5_4\end{bmatrix}$, ψ_{p_i}s and ψ_{shared}. Once again rewriting the Bayesian formula for n_r realizations of the full model with n_i observations for each realization we have:

$$\pi(\underline{\psi}, \underline{a}^5|\underline{z}) \propto \pi(\underline{z}|\underline{\psi}, \underline{a}^5)\pi(\underline{\psi})\pi(\underline{a}^5), \quad (55)$$

where $\pi(\underline{\psi})$ denotes the prior for the spatial correlation parameters and $\pi(\underline{a}^5)$ denotes the prior for the coefficients of the shared latent GP. Furthermore, $\underline{z}$ denotes the vector that includes the observation vector for the all n_r realizations (i.e. $\underline{z}^r = \begin{bmatrix}\underline{z}^r_{r_a} & \underline{z}^r_{r_b} & \underline{z}^r_{r_c} & \underline{z}^r_{r_o}\end{bmatrix}^T$). The final form of Eq. (55) reads as:

$$\pi(\underline{\psi}, \underline{a}^5|\underline{z}) \propto \prod_{r=1}^{n_r} c(\Big[\underline{v}_{\underline{z}^r_{r_a}}\ \underline{v}_{\underline{z}^r_{r_b}}\ \underline{v}_{\underline{z}^r_{r_c}}\ \underline{v}_{\underline{z}^r_{r_o}}\Big]^T |\underline{\underline{\Gamma}}_{C_{\text{SLFM}}}) \prod_{i=1}^{n_i} \pi_{r_a}((\underline{z}^r_{r_a})_i)\pi_{r_b}((\underline{z}^r_{r_b})_i)\pi_{r_c}((\underline{z}^r_{r_c})_i)\pi_{r_o}((\underline{z}^r_{r_o})_i)\pi(\underline{\psi})\pi(\underline{a}^5). \quad (56)$$

Similar to the ICM case $\pi_{r_a}(\cdot)$, $\pi_{r_b}(\cdot)$, $\pi_{r_c}(\cdot)$ and $\pi_{r_o}(\cdot)$ denote the marginal univariate PDFs given by Eq. (41), $(\underline{v}_{\underline{z}^r_{r_a}})_i$, $(\underline{v}_{\underline{z}^r_{r_b}})_i$, $(\underline{v}_{\underline{z}^r_{r_c}})_i$ and $(\underline{v}_{\underline{z}^r_{r_o}})_i$ denote the values of the corresponding CDFs at $(\underline{z}^r_{r_a})_i$, $(\underline{z}^r_{r_b})_i$, $(\underline{z}^r_{r_c})_i$ and $(\underline{z}^r_{r_o})_i$, $c(\cdot|\cdot)$ is given in Eq. (25), $\underline{\underline{\Gamma}}_{C_{\text{SLFM}}}$ denotes the correlation matrix corresponding to $\underline{\underline{K}} = \sum_{i=1}^{5} \underline{\underline{B}}^i \otimes \underline{\underline{K}}_{\delta^i}$ as given in Eq. (36). Note that $(\underline{\underline{K}}_{\delta^i})_{lm} = \Big(1 + \frac{\sqrt{3}|(x_1)_l - (x_1)_m|}{\psi_{p_i}}\Big)\exp\Big(-\frac{\sqrt{3}|(x_1)_l - (x_1)_m|}{\psi_{p_i}}\Big)$ where p_i is r_a, r_b, r_c or r_o for $i = 1, \cdots, 4$ respectively and $(\underline{\underline{K}}_{\delta^5})_{lm} = \Big(1 + \frac{\sqrt{3}|(x_1)_l - (x_1)_m|}{\psi_{\text{shared}}}\Big)\exp\Big(-\frac{\sqrt{3}|(x_1)_l - (x_1)_m|}{\psi_{\text{shared}}}\Big)$.

7. Results

This section concentrates on the results of the study. It is subdivided in three subsections. First, the results of the deterministic identification of the parameter fields for each strut are concisely presented. Second, the identified parameters of the univariate marginal PDF of each field are presented, as they are independent of the formulation to describe the correlation between the fields. Third, the results focusing on the responses of the beam model are presented. This last part includes a forward study (for a single strut, not for a network of struts) in which realizations of the final posteriors are used by the beam simulation to predict center line displacements and rotations, as well as reaction forces and moments. These are compared to those predicted by 994 validation FE simulations.

7.1. Deterministic identification results of the six struts

In this subsection, the results of the deterministic identification for each of the six struts are presented (obtained with the deterministic approach discussed in Sections 2, 3 and 6.1). Only the center line results are presented, since the reaction forces and moments are scalars that match within a couple of percent.

In Fig. 3, the center line displacements and rotations present in the objective function of Eq. (15) are shown for each of the six struts. These center line results are presented relative to those of the homogeneous case (without any

randomness). The center line profiles match well. They are especially accurate for uniaxial elongation and torsion as the applied deformation modes.

The reason for the good match of the torsion results is that regardless of the values of the geometrical parameters, Poisson's ratio of each beam element alone is used to match the rotations around the axial direction during torsion (i.e. the x_1-direction, $\Delta\omega_1^t$). The reason for the excellent match of the uniaxial elongation results is that only the cross sectional area is relevant and not the true shape. The reason that the remaining results do not perfectly match is that the true cross sectional shape is important, and the cross sectional parametrization of the beams is not the same as used in the FE simulations (which was done on purpose, as this is also not known if the FE simulations would be based on experimentally characterized geometries).

The identified parameter fields associated with the center line results in Fig. 3 are presented in Fig. 4 and serve as the 'observations' for the probabilistic identification ($\underline{z}$). All parameter fields, except the fields of r_o, show that some boundary effect occurs, because the displacement boundary conditions in the FE simulations are applied to all the nodes at the ends.

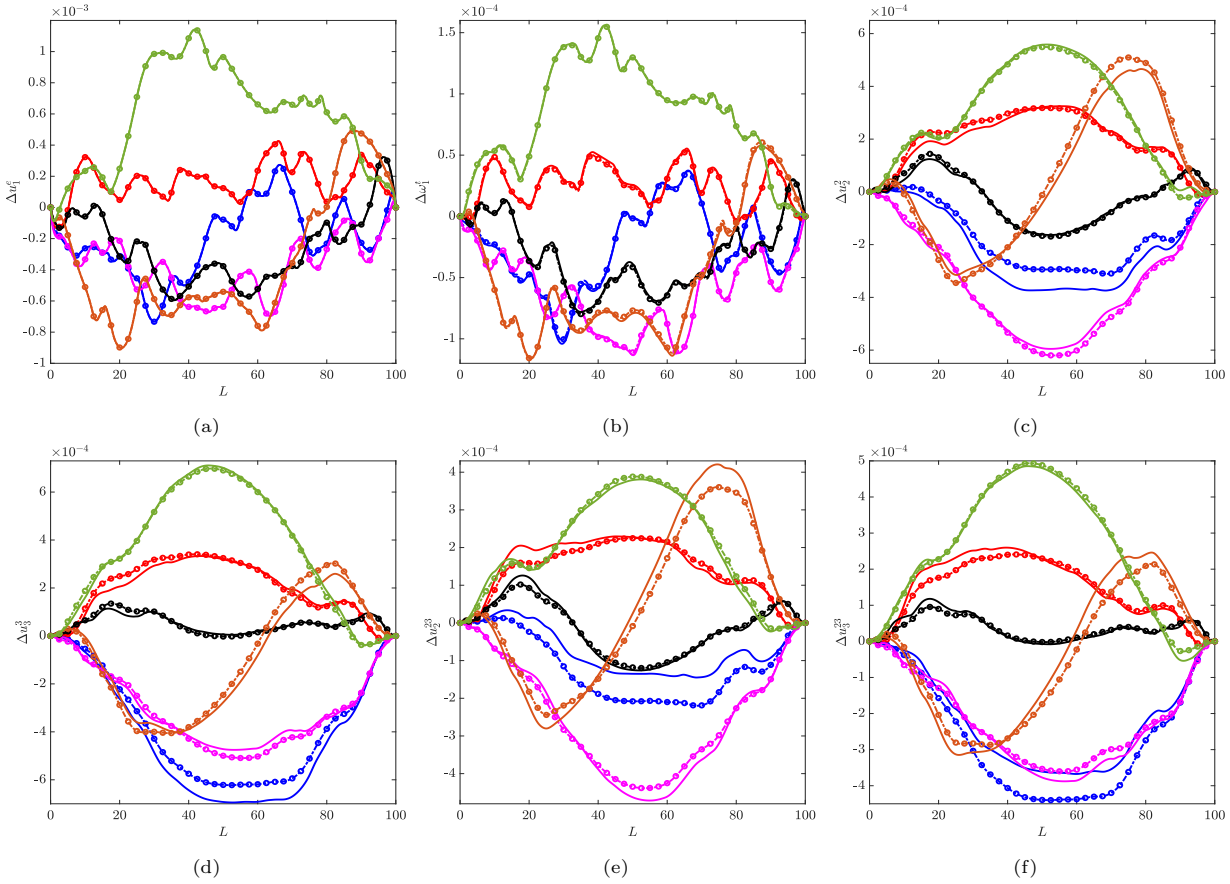

Figure 3: The final differences between the relative center line displacements and rotations of the FE simulations (sold lines) and the beam simulations (dashed lines with circles) for the six struts. The results are presented relative to those of the homogeneous case. The colors denote the different struts. The subscripts refer to the three directions and the superscripts refer to the five applied deformation modes (e: axial elongation, t: torsion, 2: nodes at one end displaced in the x_2-direction, 3: nodes at one end displaced in the x_3-direction, and 23: nodes at one end simultaneously displaced in the x_2-direction and x_3-direction).

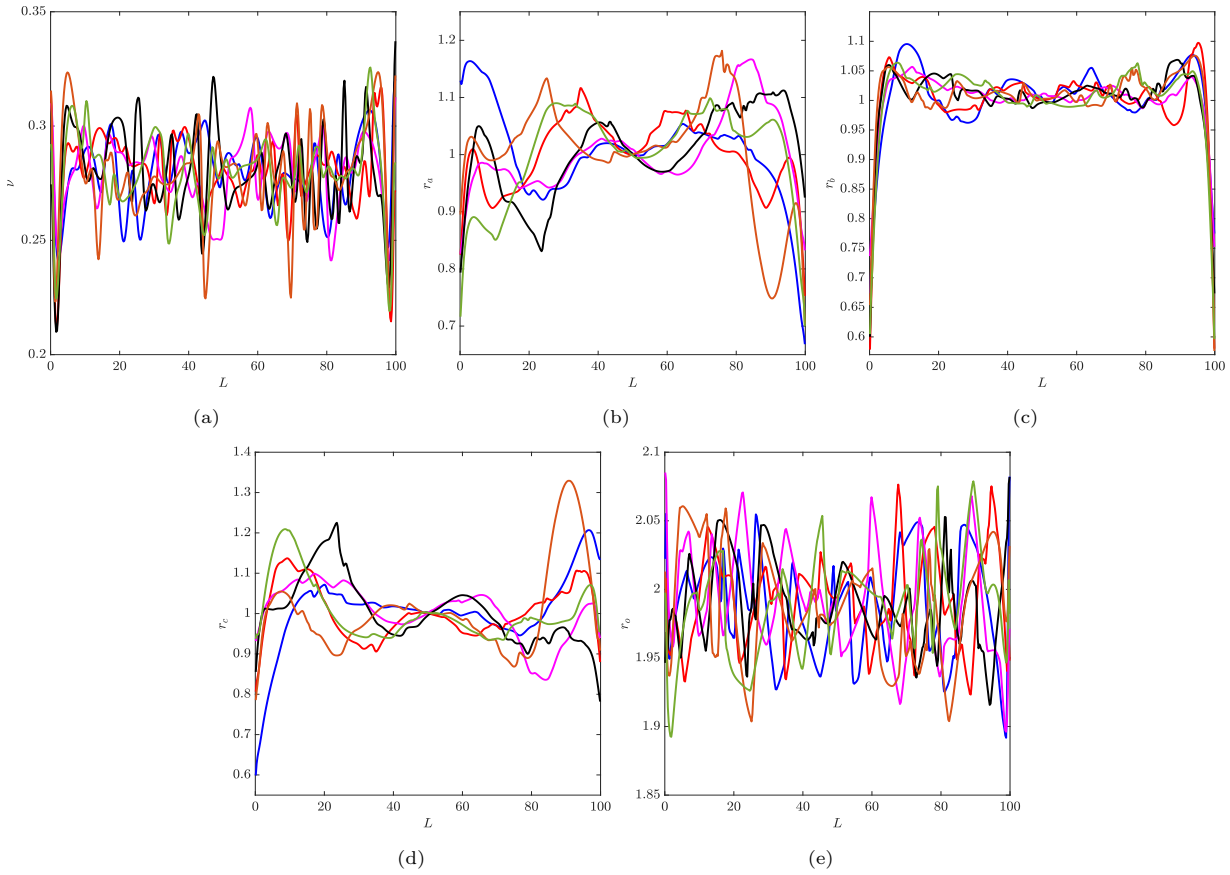

Figure 4: Deterministically identified input fields for the beam representations of the six struts. The colors denote the different struts.

7.2. Results for the univariate marginal PDFs

7.2.1. Poisson's ratio

The univariate marginal PDF for Poisson's ratio is governed by two bounds and two shape parameters. As the bounds are set, only the two shape parameters are to be identified: $\underline{p}_\nu = \begin{bmatrix}\alpha_\nu & \beta_\nu\end{bmatrix}^T$. The selected prior for both of the shape parameters is a modified Gaussian:

$$\pi(p_\nu) \propto \begin{cases} \exp\Big(-\frac{(p_\nu - \overline{p}_\nu^{\text{prior}})^2}{2s_{p_\nu}^{\text{prior}\,2}}\Big) & \text{if } p_\nu \geq 0 \\ 0 & \text{otherwise} \end{cases}, \tag{57}$$

where p_ν denotes either α_ν or β_ν and $\overline{p}_\nu^{\text{prior}}$ and $s_{p_\nu}^{\text{prior}}$ denote the mean value and the standard deviation of the Gaussian distribution from which the prior is modified. The selected values for the prior parameters are reported in Table 1, which are selected based on the mean value and standard deviation of the observations.

The Metropolis algorithm with an adaptive proposal distribution [69] is used to sample the posterior and to obtain its desired statistical summaries such as the mean values, the MAP estimates and the posterior covariance matrix. To this end, 100×10^3 samples are drawn from the posterior and the first 30% are burned. Table 2 gives the values of the MAP estimates for the parameters describing the marginal univariate PDFs.

The 2400 deterministically identified Poisson's ratios (the six fields in Fig. 4(a)) are presented as a single PDF in Fig. 5(a) (solid black line). Also presented in the same diagram, are the PDFs associated with 100 sampling points randomly selected from the 95% credible region (i.e. the region that one believes 95% it contains true value of some parameter [71]) and the PDF associated with the MAP estimate. The results show a reasonable match. Only the MAP estimate is used in the remainder of the identification.

Table 1: The selected values for the parameters defining the priors of the univariate marginal PDFs.

$\overline{\alpha}_{\nu}^{\text{prior}}$	1164.7315	$\overline{\alpha}_{r_c}^{\text{prior}}$	11.1245
s_{α_ν}	388.2483	$s_{\alpha_{r_c}}$	5.5623
$\overline{\beta}_{\nu}^{\text{prior}}$	582.4815	$\overline{\theta}_{r_c}^{\text{prior}}$	1.0427
s_{β_ν}	194.1605	$s_{\theta r_c}$	0.5213
$\overline{\alpha}_{r_a}^{\text{prior}}$	15.3904	$\overline{\alpha}_{r_o}^{\text{prior}}$	59.7961
$s_{\alpha_{r_a}}$	7.6952	$s_{\alpha_{r_o}}$	29.8981
$\overline{\theta}_{r_a}^{\text{prior}}$	1.0376	$\overline{\theta}_{r_o}^{\text{prior}}$	2.0067
$s_{\theta_{r_a}}$	0.5188	$s_{\theta_{r_o}}$	1.0034
$\overline{\alpha}_{r_b}^{\text{prior}}$	31.1125		
$s_{\alpha_{r_b}}$	15.5563		
$\overline{\theta}_{r_b}^{\text{prior}}$	1.0245		
$s_{\theta_{r_b}}$	0.5123		

Table 2: The MAP estimates for the parameters describing the univariate marginal PDFs.

$\alpha_{\nu}^{\text{MAP}}$	1171.9988	$\alpha_{r_c}^{\text{MAP}}$	11.1251
β_{ν}^{MAP}	586.1201	$\theta_{r_c}^{\text{MAP}}$	1.0427
$\alpha_{r_a}^{\text{MAP}}$	15.3916	$\alpha_{r_o}^{\text{MAP}}$	59.8016
$\theta_{r_a}^{\text{MAP}}$	1.0376	$\theta_{r_o}^{\text{MAP}}$	2.0067
$\alpha_{r_b}^{\text{MAP}}$	31.1122		
$\theta_{r_b}^{\text{MAP}}$	1.0245		

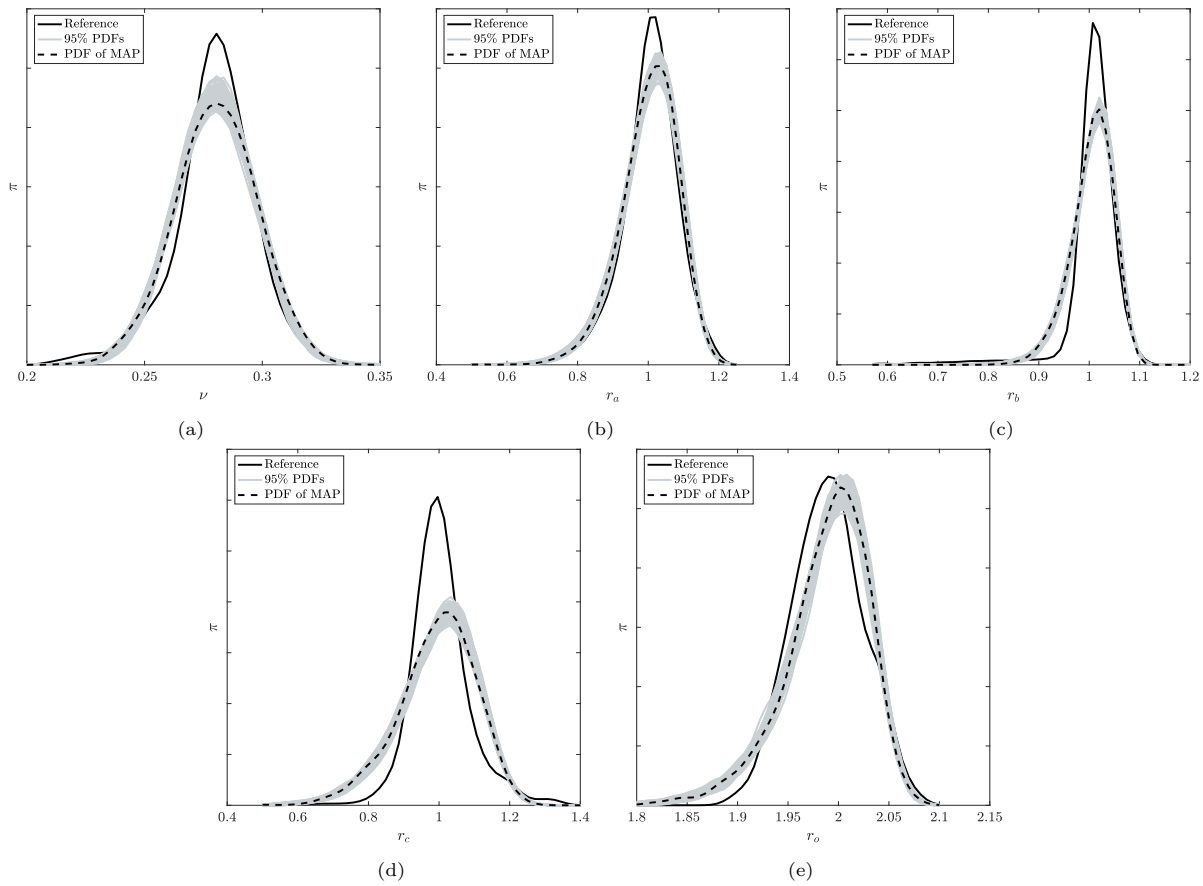

Figure 5: Results for the univariate marginal PDFs. The reference results are the results of the deterministic identification s(based on 2400 observations per parameter). The grey lines are PDFs associated with the 95% credible region (i.e. the region that one believes 95% it contains true value of some parameter [71]). The dashed line is the PDF associated with the MAP estimate. This graphical test [9] shows a reasonable agreement between the simulated curves and the ones based on observations.

7.2.2. Geometrical parameters

As mentioned in Subsection 6.2.2, the parameters to be identified for the univariate marginal PDF of the geometrical parameters are $\underline{p}_{p_i} = \begin{bmatrix} \alpha_{p_i} & \theta_{p_i} \end{bmatrix}$ with p_i being r_a, r_b, r_c or r_o. Similar to the case for Poisson's ratio, the number of observations for each geometrical parameter is 2400. The priors are again selected in the form of Eq. (57), with the prior parameters reported in Table 1. The posteriors are again evaluated using 100×10^3 samples and the first 30% of the samples are burned. Fig. 5(b)-5(e) shows the PDFs associated with the deterministically identified parameters, the PDFs associated with 100 samples randomly drawn from the 95% credible region and the PDF associated with the MAP estimate. It shows a reasonable agreement. The MAP estimates for the parameters of the univariate marginal PDFs furthermore, are given in Table 2.

7.3. Results for the random fields

Once the univariate marginal PDFs are identified, the MAP estimates (Table 2) are used as the known (and constant) inputs for the identification of the random fields. In order to avoid numerical instabilities due to the fact that the axial locations are substantially close to each, the parameter set of not all 400 axial locations is employed, but one parameter set per four axial locations, i.e. $n_i = 100$ and $n_r = 6$ in Eqs. (46), (50), (54) and (56). Similar to the identification of the univariate marginal PDFs' parameters, the Metropolis algorithm with an adaptive proposal distribution is used to approximate the posterior distribution with 100×10^3 samples of which the first 30% are burned.

In order to study the performance of the discussed models, the samples of the parameter fields are randomly selected and propagated in the beam simulations. The center line displacements and rotations and reaction forces and moments are then compared to those predicted by 994 FE simulations. The same center line results are presented as are employed in the objective functions of Eq. (15). Also similar to the presentation in Subsection 7.1, is that the *relative* center line results are presented, i.e. the results are corrected with those expected from the homogeneous case. The presented reaction forces and moments are in accordance with the applied deformation modes.

7.3.1. Poisson's ratio

The random field of Poisson's ratio is modeled independently from the other fields in each formulation. This entails that a single parameter is required for this field: length scale parameter ψ_ν. The prior for ψ_ν is chosen to be a uniform distribution with bounds 0.25 and 100. The value of 0.25 for the lower bound is chosen since it is the distance between two consecutive axial locations. The value of 100 for the upper bound is chosen since it is the total length of a strut. The posterior is sampled in the same way as all other posteriors.

7.3.2. Geometrical parameters

(A) Independent fields. The parameters to be identified in case of independent fields are the length scale parameter of each field: ψ_{p_i} with p_i being r_a, r_b, r_c and r_o (see Eq. (48)). Exactly the same priors are selected as for the length scale parameter of Poisson's ratio, with the same bounds. The same sampling approach is applied.

In order to compare the results of the independent field model, 994 samples for the five length scale parameters (ψ_ν and ψ_{p_i}) are drawn from the posteriors and together with the MAP estimates for the univariate marginal PDFs' parameters used in the independent field model, from which realizations for the five input fields are drawn. These realizations of input fields are used in the beam simulation to obtain the center line results that are compared to the center line results of 994 FE simulations.

Figs. 6(a)-(b) to 11(a)-(b) present the same relative center line results as in Eq. (15) predicted by the beam simulations and by the FE simulations for each of the five applied deformation modes. The diagrams on the left show the mean, bounds and interval of both the beam simulations and the FE simulations and the diagrams on the right show a small number of predicted fields. A visual inspection of these results indicates a reasonable agreement of the bounds, of the mean and of the length scale present in the single fields. Generally speaking, the interval of the FE results remains within the interval of the beam results. However, at some axial locations the observations are outside the prediction bounds. This is mainly the case for the torsion test.

(B) Intrinsic coregionalization model. The parameters to be identified in the ICM model are a single length scale parameter, ψ_δ, and the six parameters in $\underline{\underline{\gamma}}_B$ of Eq. (54). The following priors are selected:

$$\pi(\psi_\delta) \propto \begin{cases} \exp\Big(- \frac{(\psi_\delta - \overline{\psi}_\delta^{\text{prior}})^2}{2 s_{\psi_\delta}^{\text{prior}\,2}} \Big) & \text{if } 0.25 \leq \psi_\delta \leq 100 \\ 0 & \text{otherwise} \end{cases}, \tag{58}$$

$$\pi((\underline{\underline{\Gamma}}_{\underline{\underline{B}}})_{ij}) \propto \begin{cases} \exp\Big(-\frac{((\underline{\underline{\Gamma}}_{\underline{\underline{B}}})_{ij}-\overline{(\underline{\underline{\Gamma}}_{\underline{\underline{B}}})}_{ij}^{\text{prior}})^2}{2{s^{\text{prior}}_{(\underline{\underline{\Gamma}}_{\underline{\underline{B}}})_{ij}}}^2}\Big) & i<j\in\ \{1,\cdots,4\}\ \text{ if }\ -1\leq(\underline{\underline{\Gamma}}_{\underline{\underline{B}}})_{ij}\leq 1 \\ 0 & \text{otherwise} \end{cases}, \tag{59}$$

where $\overline{\psi}_{\delta}^{\text{prior}}=6$, $s_{\psi_\delta}^{\text{prior}}=3$, $\overline{(\underline{\underline{\Gamma}}_{\underline{\underline{B}}})}_{ij}^{\text{prior}}=0, i<j\in\ \{1,\cdots,4\}$ and $s^{\text{prior}}_{(\underline{\underline{\Gamma}}_{\underline{\underline{B}}})_{ij}}=0.3333$. Note, that $\overline{\psi}_{\delta}^{\text{prior}}$ is chosen to be average of the mean estimates for the parameters identified in the independent fields case.

The prediction intervals for the ICM approach alongside the observations are shown in Figs. 6(c)-(d) to 11(c)-(d). The results seem at first sight similar to those of the independent fields: similar length scales seem to be present in the different types of results for the different applied deformation modes and the mean and the interval bounds are similar. However, the interval associated with the ICM model consistently encompasses the interval of the FE results, whereas this is not always the case for the formulation employing independent fields.

(C) Semiparametric latent factor model. As mentioned before, an alternative way to model the representative random fields of the geometrical parameters is to model each parameter field as an independent random field plus a shared random field that correlates these fields to each other. Once this modeling approach is formulated mathematically (see Subsection 6.3.2) it leads to an SLFM model with ψ_{p_i}s, a single ψ_{shared} and $\underline{a}^5$, where p_i can be r_a, r_b, r_c or r_o and $\underline{a}^5$ denotes the column with the coefficients of the shared random field. We choose the priors in the modified form of the Gaussian distribution (see Eq. (58)) with the defining values given in Table 3. Note that we have chosen the values for $\overline{\psi}_{p_i}^{\text{prior}}$ based on the result for the independent fields. Furthermore, we choose $\overline{\psi}_{\text{shared}}^{\text{prior}}$ to be the mean value of the identified length scale for the ICM approach.

Table 3: The selected values for the parameters defining the priors for the SLFM approach.

${}^3\overline{\psi}_{r_a}^{\text{prior}}$	8.1483	${}^4\overline{a}_1^{5\,\text{prior}}$	0
$s_{\psi_{r_a}}$	4.0742	$s_{a_1^5}$	5
$\overline{\psi}_{r_b}^{\text{prior}}$	4.5487	$\overline{a}_2^{5\,\text{prior}}$	0
$s_{\psi_{r_b}}$	2.2744	$s_{a_2^5}$	5
$\overline{\psi}_{r_c}^{\text{prior}}$	10.6418	$\overline{a}_3^{5\,\text{prior}}$	0
$s_{\psi_{r_c}}$	5.3209	$s_{a_3^5}$	5
$\overline{\psi}_{r_o}^{\text{prior}}$	2.2873	$\overline{a}_4^{5\,\text{prior}}$	0
$s_{\psi r_o}$	1.1437	$s_{a_4^5}$	5
$\overline{\psi}_{\text{shared}}^{\text{prior}}$	3.5872		
$s_{\psi_{\text{shared}}}$	1.7936		

The prediction intervals as well as the observations for the SLFM approach are presented in Fig. 6(e) to Fig. 11(e). These figures show that the SLFM approach leads to prediction intervals that are wider than those of the independent fields but narrower than those of the ICM approach. Similar to the previous cases, samples the responses of the beam model are presented alongside sample responses of the FE model in Fig. 6(f) to Fig. 11(f).

Moreover, comparing Figs. 8, 9, 10 and 11 one can see that the predicted lateral displacements in both x_2 (i.e. u_2) and x_3 (i.e. u_3) are similar for all approaches.

A general comparison of Figs. 6 to 11 shows that the ICM approach leads to prediction intervals that cover the FE responses for all the tests. The SLFM approach leads to prediction intervals that are wider than the independent random fields and fully cover the FE responses for all the tests except the axial torsion case.

The reference PDFs for the reaction forces and moments are shown in Fig. 12 as well as 100 PDFs associated with the 95% credible region. Generally speaking one can see that the PDFs associated with the ICM approach are wider than the two other approaches. Furthermore, for all the three methods the MAP estimate is close to the peaks of the reference PDFs. However, in general one can say that both the independent fields and the SLFM approaches perform better than the ICM approach.

[3] Length scales are bounded between 0.25 and 100.

[4] $i=1,\cdots,4$ in $\overline{a}_i^5$ denote r_a, r_b, r_c, r_o respectively.

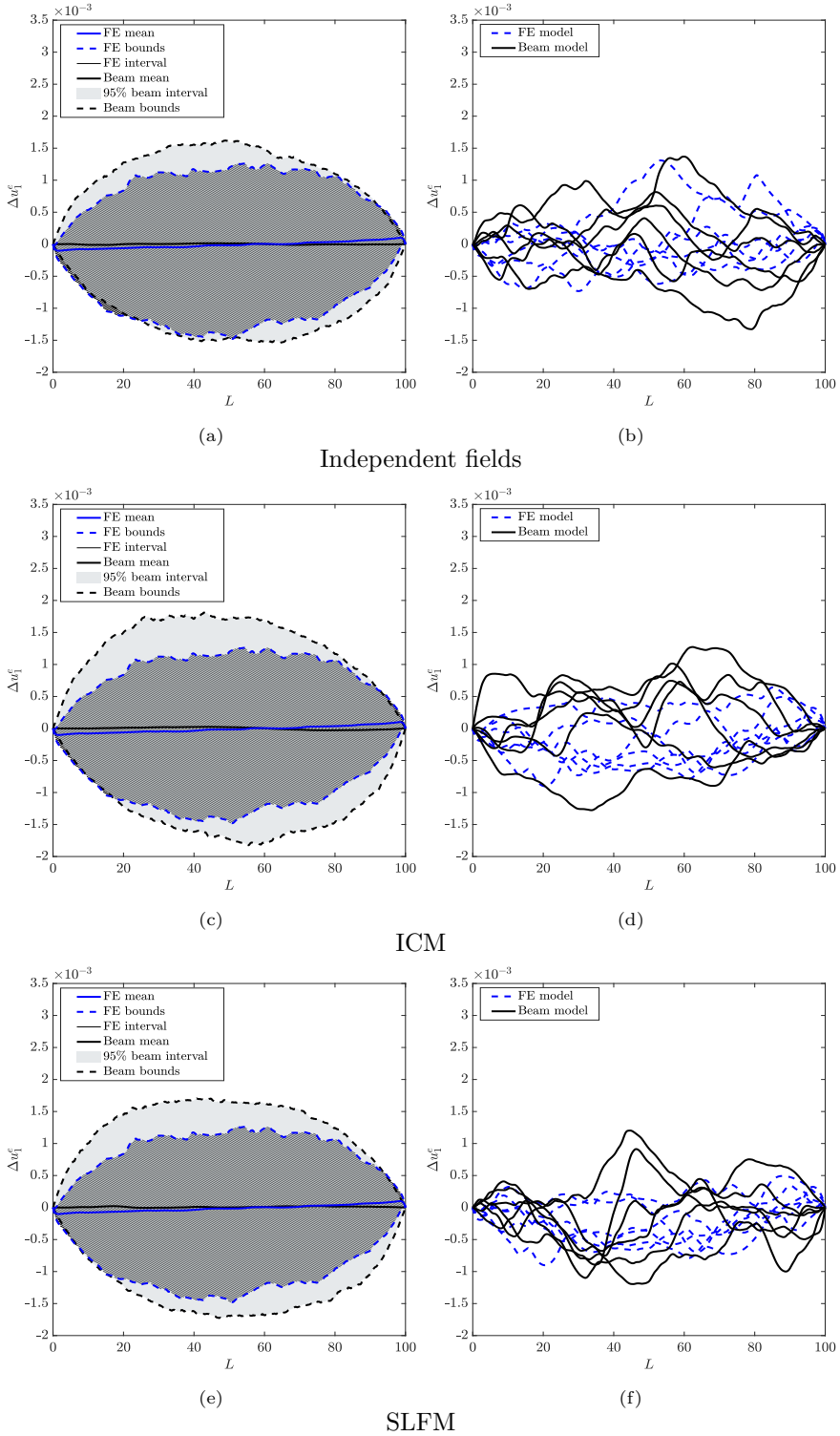

Figure 6: Elongation: prediction intervals and observation intervals when the parameter fields are modeled as (a) independent random fields, (c) correlated random fields using the ICM approach and (e) correlated random fields using the SLFM approach. (b), (d) and (f) show samples of the FE model response and of the beam model response. One can see that in both the ICM and the SLFM approaches the observations at all locations are inside the prediction intervals. However, in the case of independent fields the observations bounds around $x_1 = 15$ are outside the predictions intervals. Furthermore, comparing (a), (c) and (e) indicates that the ICM approach has the widest prediction interval and the independent fields approach has the narrowest prediction interval. Although the difference between the ICM approach and the SLFM approach for this test is not large. Moreover, the sample curves in (b), (d) and (f) show that the beam responses are similar to the FE responses. Note that the presented responses are relative to that of the homogeneous case.

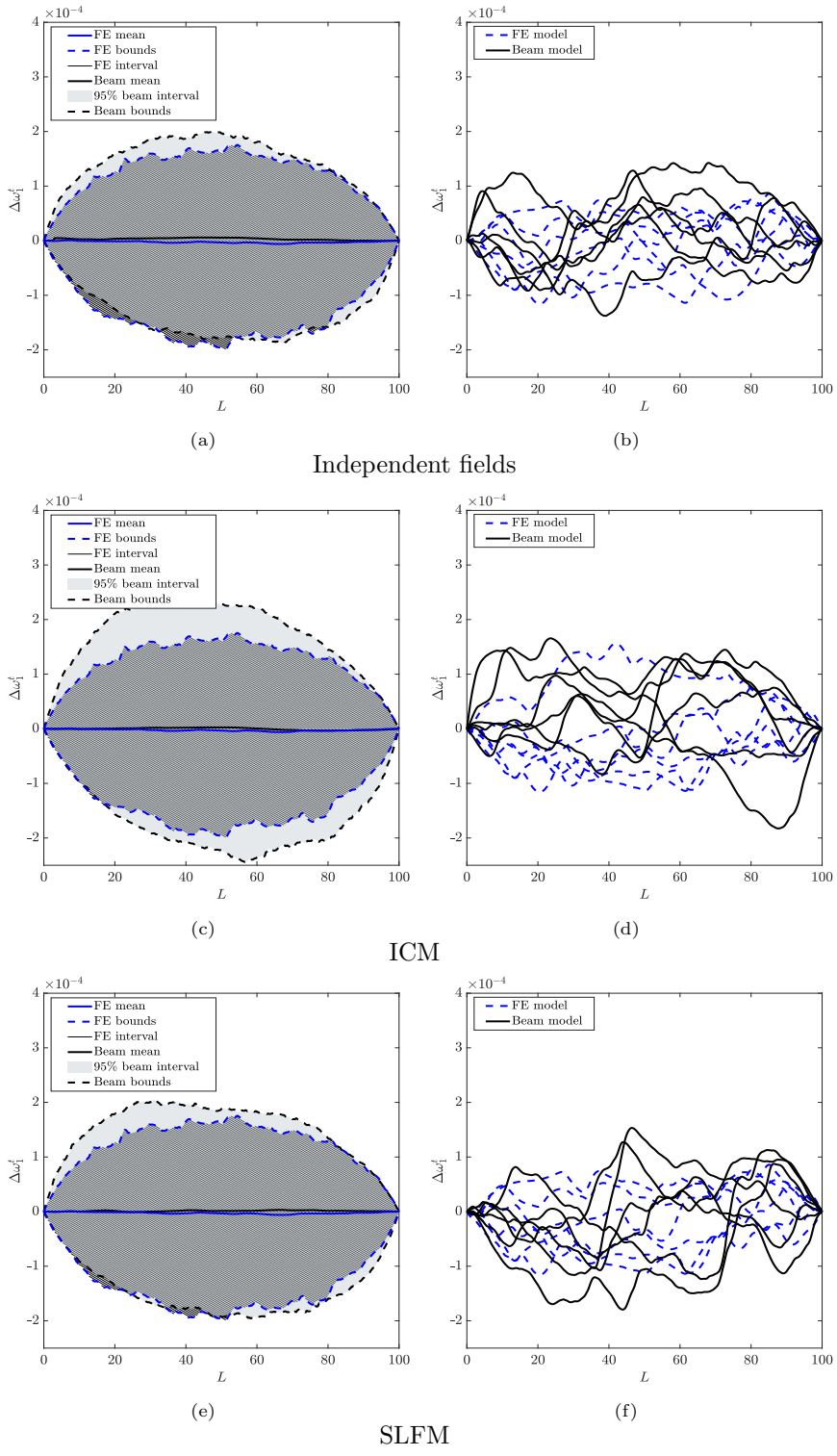

Figure 7: Torsion: prediction intervals and observation intervals when the parameter fields are modeled as (a) independent random fields, (c) correlated random fields using the ICM approach and (e) correlated random fields using the SLFM approach. A few sample responses of the FE models and of the beam models are shown in the diagrams on the right. The FE responses only remain the prediction interval of the ICM approach. Moreover, similar to axial elongation, the ICM approach has the widest prediction interval whereas the independent fields approach has the narrowest prediction interval. Note that the presented responses are relative to that of the homogeneous case.

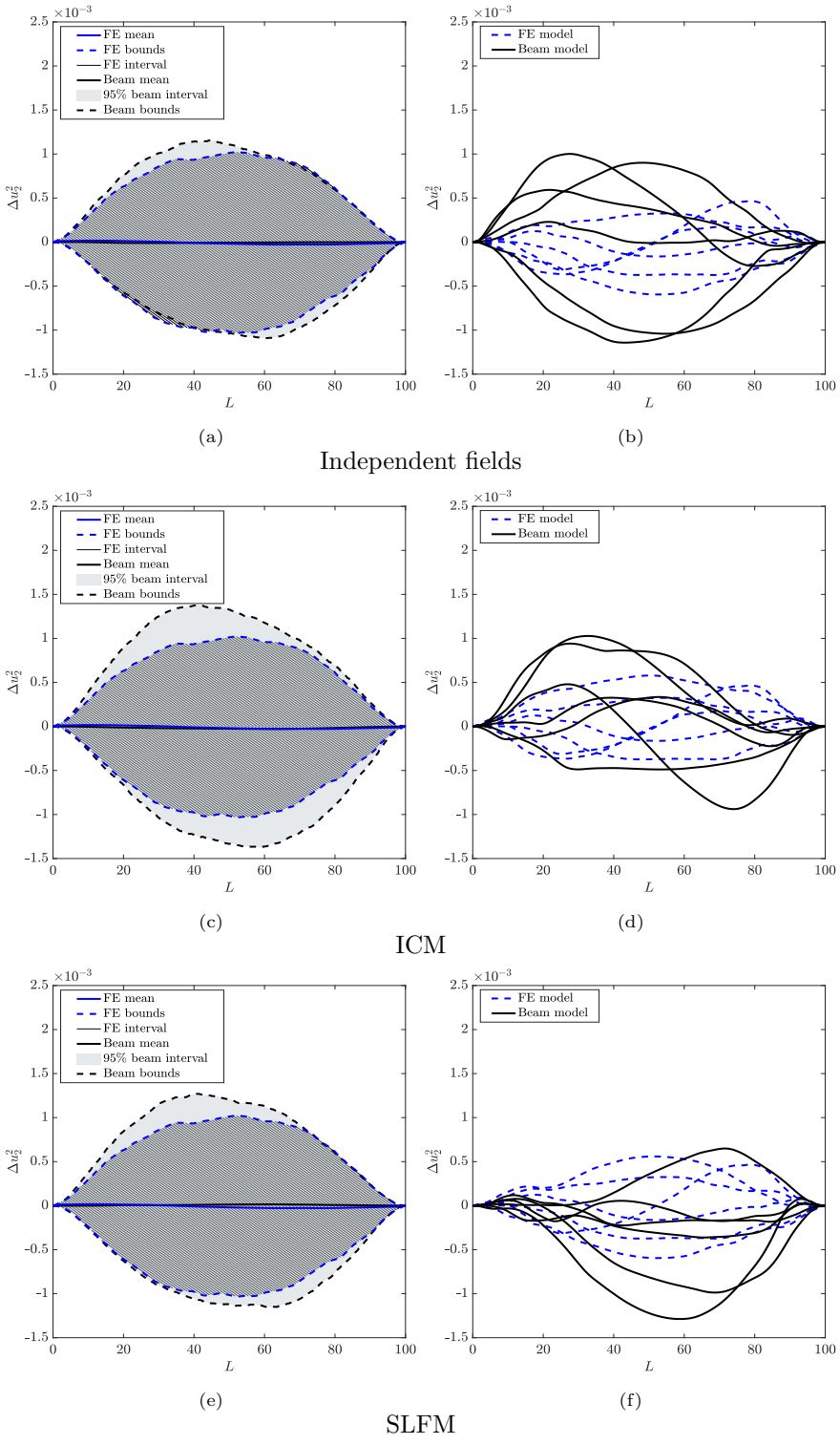

Figure 8: Displacement applied in direction of x_2: prediction intervals and observation intervals when the parameter fields are modeled as (a) independent random fields, (c) correlated random fields using the ICM approach and (e) correlated random fields using the SLFM approach. A few sample responses of the FE models and of the beam models are shown in the diagrams on the right. The FE results are within the predictions intervals of both the ICM and SLFM approach. However, the prediction interval of the ICM approach is clearly wider than that of the SLFM approach. Note that the presented responses are relative to that of the homogeneous case.

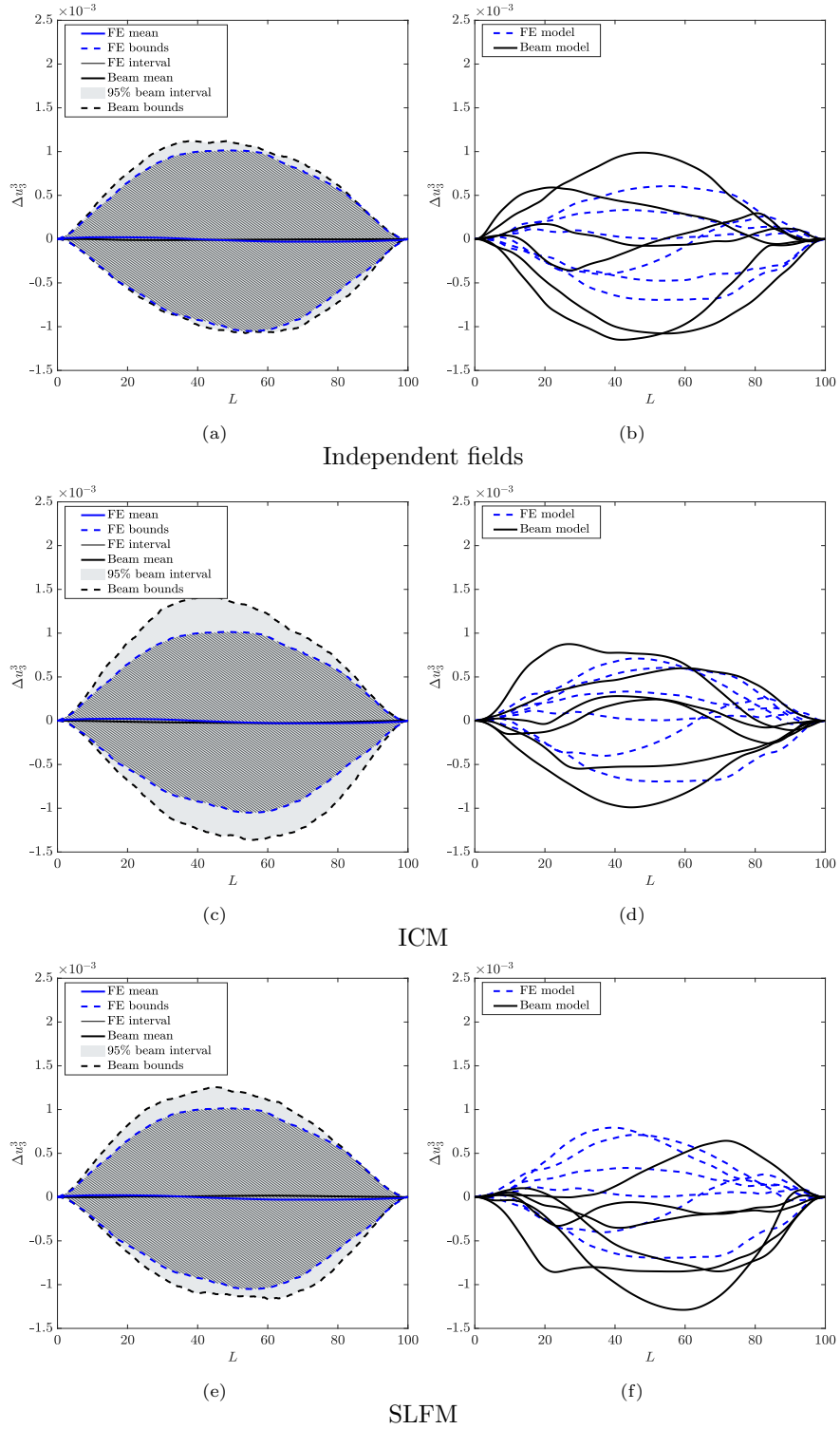

Figure 9: Displacement applied in direction of x_3: prediction intervals and observation intervals when the parameter fields are modeled as (a) independent random fields, (c) correlated random fields using the ICM approach and (e) correlated random fields using the SLFM approach. A few sample responses of the FE models and of the beam models are shown in the diagrams on the right. The prediction intervals of all three formulations encompass the FE results. The ICM approach has the widest prediction interval and the independent fields approach has the narrowest prediction interval which is slightly wider than that of the FE results. Note that the presented responses are relative to that of the homogeneous case.

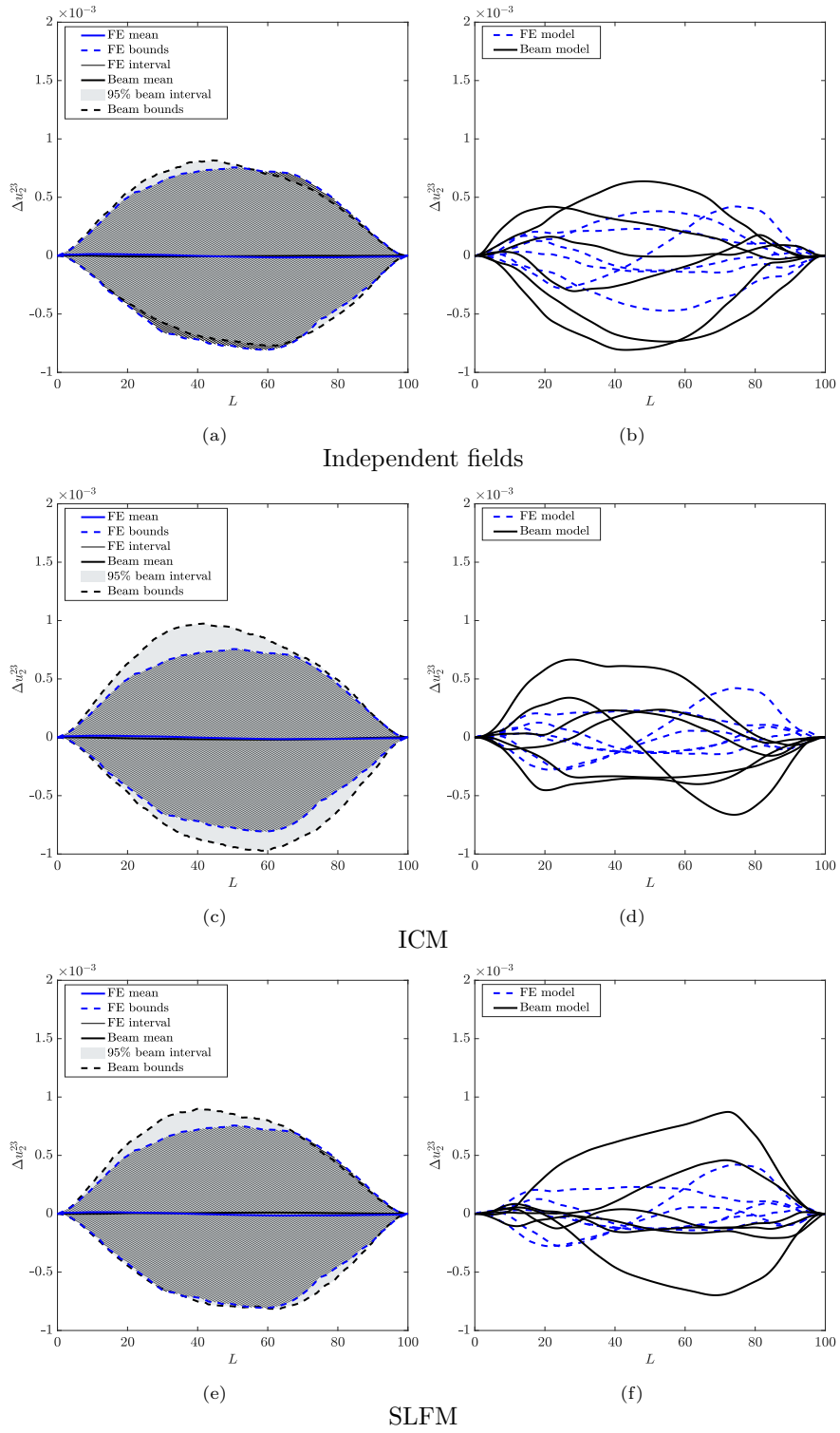

Figure 10: Bending applied in both x_2 and x_3 simultaneously, lateral displacement in x_2: prediction intervals and observation intervals when the parameter fields are modeled as (a) independent random fields, (c) correlated random fields using the ICM approach and (e) correlated random fields using the SLFM approach. A few sample responses of the FE models and of the beam models are shown in the diagrams on the right. The prediction intervals of both the ICM approach and the SLFM approach encompass all the FE results. However, the ICM approach yields a wider prediction interval than the SLFM approach. Note that the presented responses are relative to that of the homogeneous case.

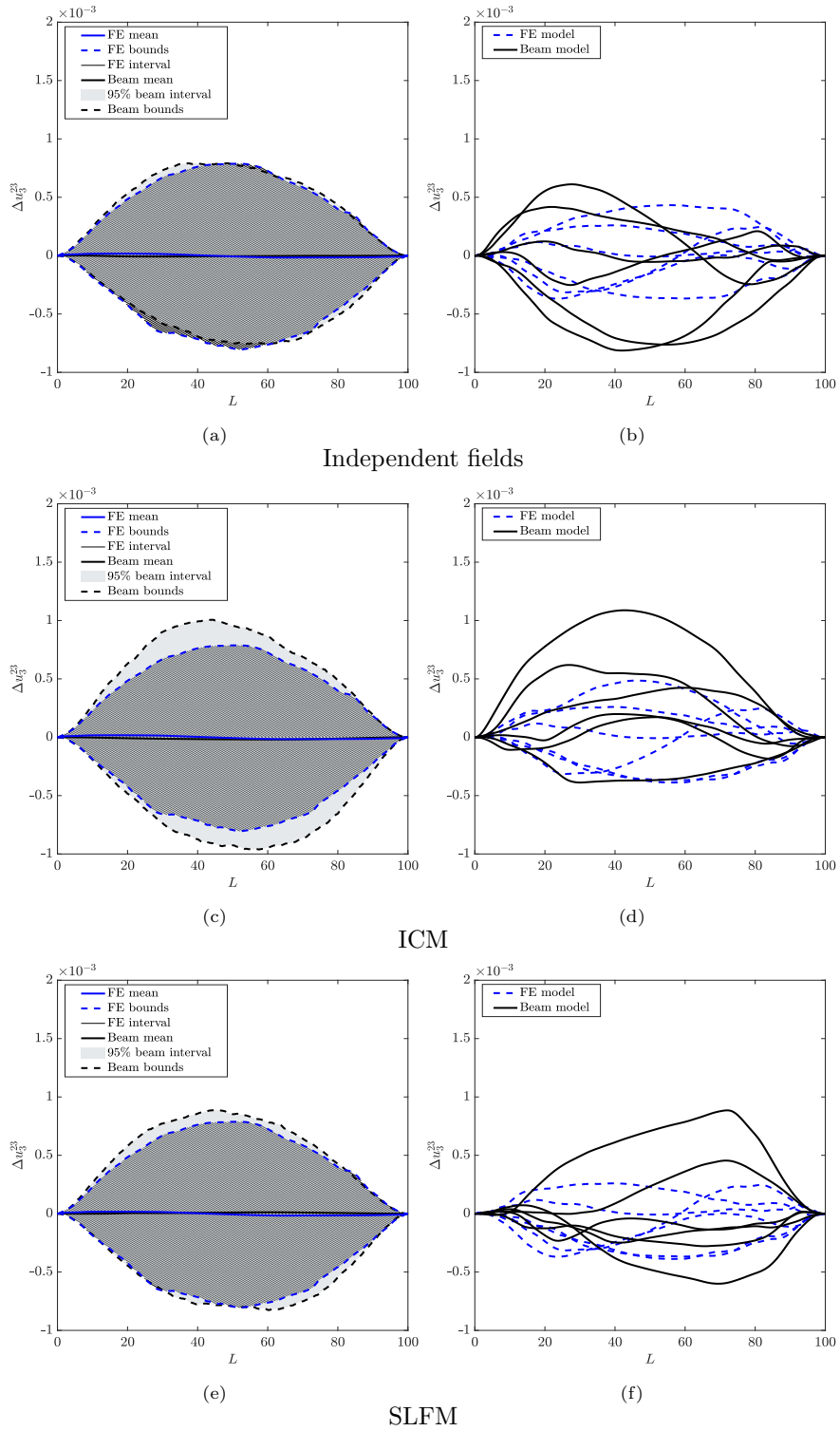

Figure 11: Bending applied in both x_2 and x_3 simultaneously, lateral displacement in x_3: prediction intervals and observation intervals when the parameter fields are modeled as (a) independent random fields, (c) correlated random fields using the ICM approach and (e) correlated random fields using the SLFM approach. A few sample responses of the FE models and of the beam models are shown in the diagrams on the right. The prediction intervals of both the ICM approach and the SLFM approach encompass all the FE results. However, the ICM approach yeilds a wider prediction interval than the SLFM approach. Note that the presented responses are relative to that of the homogeneous case.

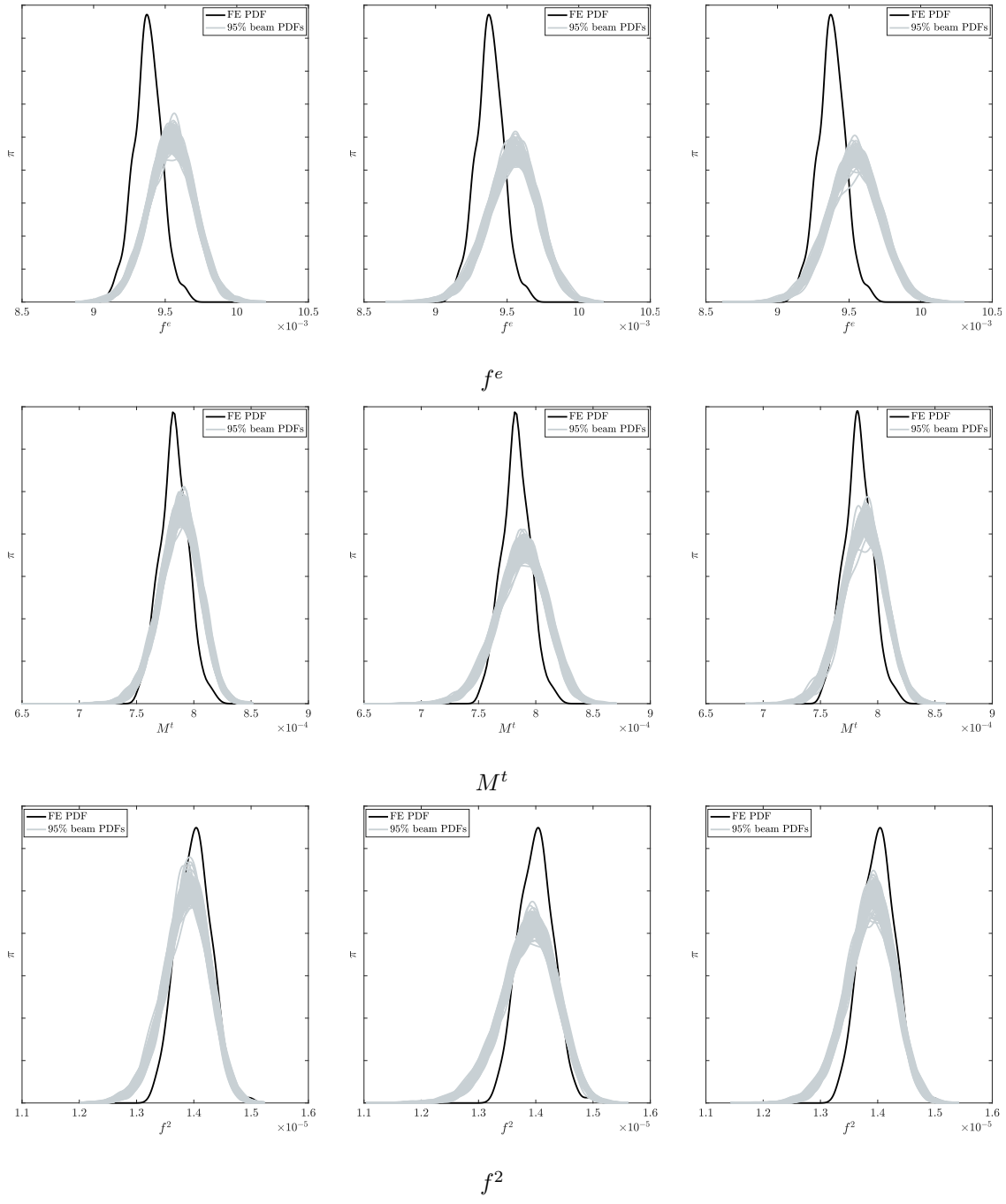

Figure 12: The FE PDFs (solid black lines) as well as the PDFs associated with 95% credible region (grey lines) for the reaction forces and moments of the different applied deformation modes (indicated by the superscript). The independent fields and the SLFM methods are more accurate than the ICM method. However, the MAP estimates of all three approaches are sufficiently close to the peaks of the FE PDFs. Furthermore, the PDFs associated with the ICM method are the widest.

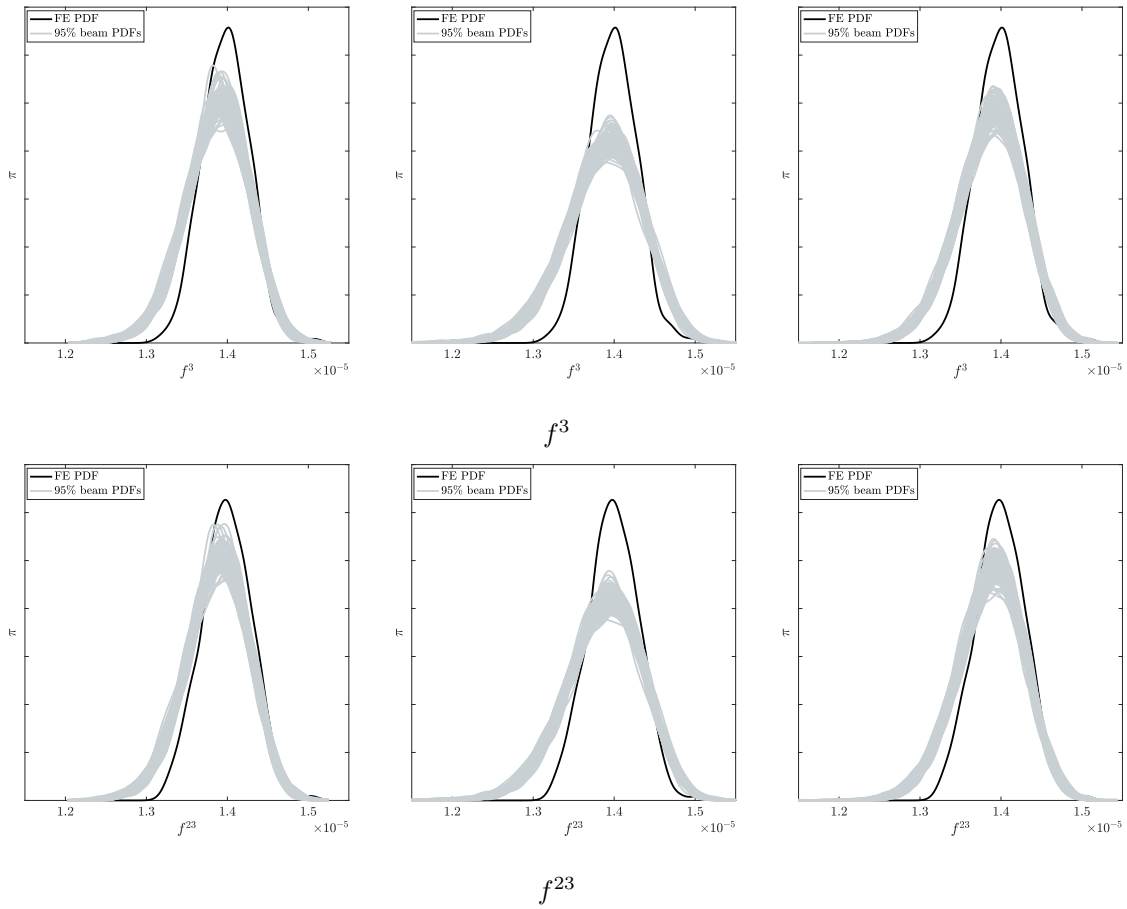

Continued Figure 12: The FE PDFs (solid black lines) as well as the PDFs associated with 95% credible region (grey lines) for the reaction forces and moments of the different applied deformation modes (indicated by the superscript). The independent fields and the SLFM methods are more accurate than the ICM method. However, the MAP estimates of all three approaches are sufficiently close to the peaks of the FE PDFs. Furthermore, the PDFs associated with the ICM method are the widest.

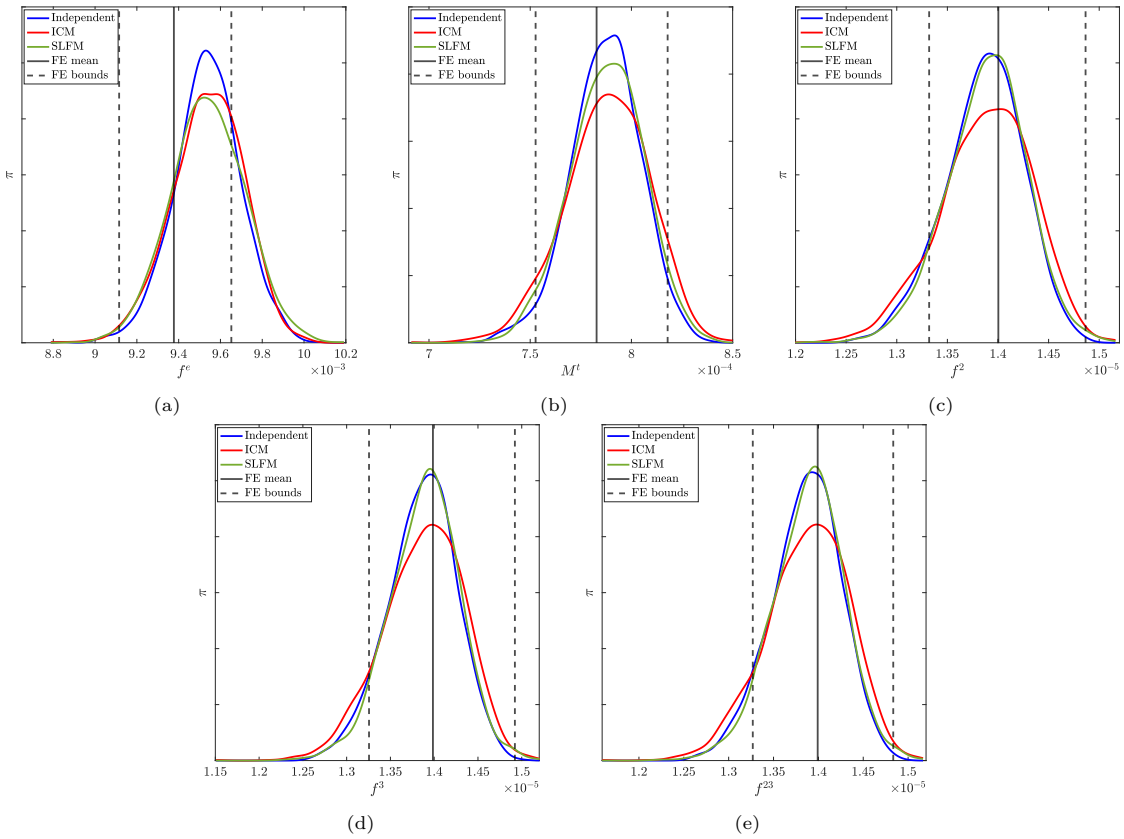

Figure 13: The PDFs for the reaction forces and moments as well as the FE values. For all the cases the reference values as well as their bounds are inside the prediction PDFs. Except for f^e and M^t the corresponding mean values of the reaction forces and moments are located at the peak of the PDFs. The independent fields yields narrowest PDFs (i.e. more certainty about the estimated values).

Fig. 13 furthermore, presents the PDFs for the reaction forces and moments corresponding to each approach alongside the means and the bounds of the reference forces and moments. One can see that for all the three approaches the reference values are inside the prediction PDFs and except for f^e and M^t the mean values are located at the peak of the PDFs. Moreover the case of independent fields yields narrower PDFs for the reaction forces and moments (i.e. more certainty about the estimated values).

7.3.3. Correlations

The previous subsection has concentrated on responses of single fields. The results in the current subsection focus on the correlations between the different fields. Figs. 6(b)-6(f) to 11(b)-11(f) show samples of the responses for both the FE and beam simulations. Comparing the curves, one can say that the reference curves are similar to the ones of the beam simulations. A more stringent comparison of the output curves is achieved by numerically calculating the autocorrelation functions [72] for the 994 FE reference curves and comparing them to those of the beam simulations. The autocorrelation bounds for the FE simulations as a function of distance between two points (ΔL) alongside the predictions are presented in Fig. 14 for the independent fields (left), ICM (middle) and SLFM (right). Generally speaking, all three autocorrelation functions are similar. However, if one considers only the prediction mean and the reference mean both for Δu_1^e and $\Delta \omega_1^t$, the independent fields and SLFM perform better than the ICM approach. For the other outputs all three approaches perform similar. However, considering the prediction intervals the ICM approach leads to a wider interval. Except for Δu_1^e and $\Delta \omega_1^t$ the prediction intervals for the ICM approach contain more of the reference observations.

Similarly the cross-correlation functions are given in Fig. 15 to assess the correlations between different outputs of both the FE and beam simulations. Note that only the cross-correlation function between Δu_1^e and $\Delta \omega_1^t$ is presented in Fig. 15, as only this one shows a difference between the three formulations. Comparing the diagrams in Fig. 15 one can see that the envelopes corresponding to independent fields (left) and SLFM (right) include all the interval associated with the FE simulations. However, for the ICM approach (middle) the FE simulations' interval is

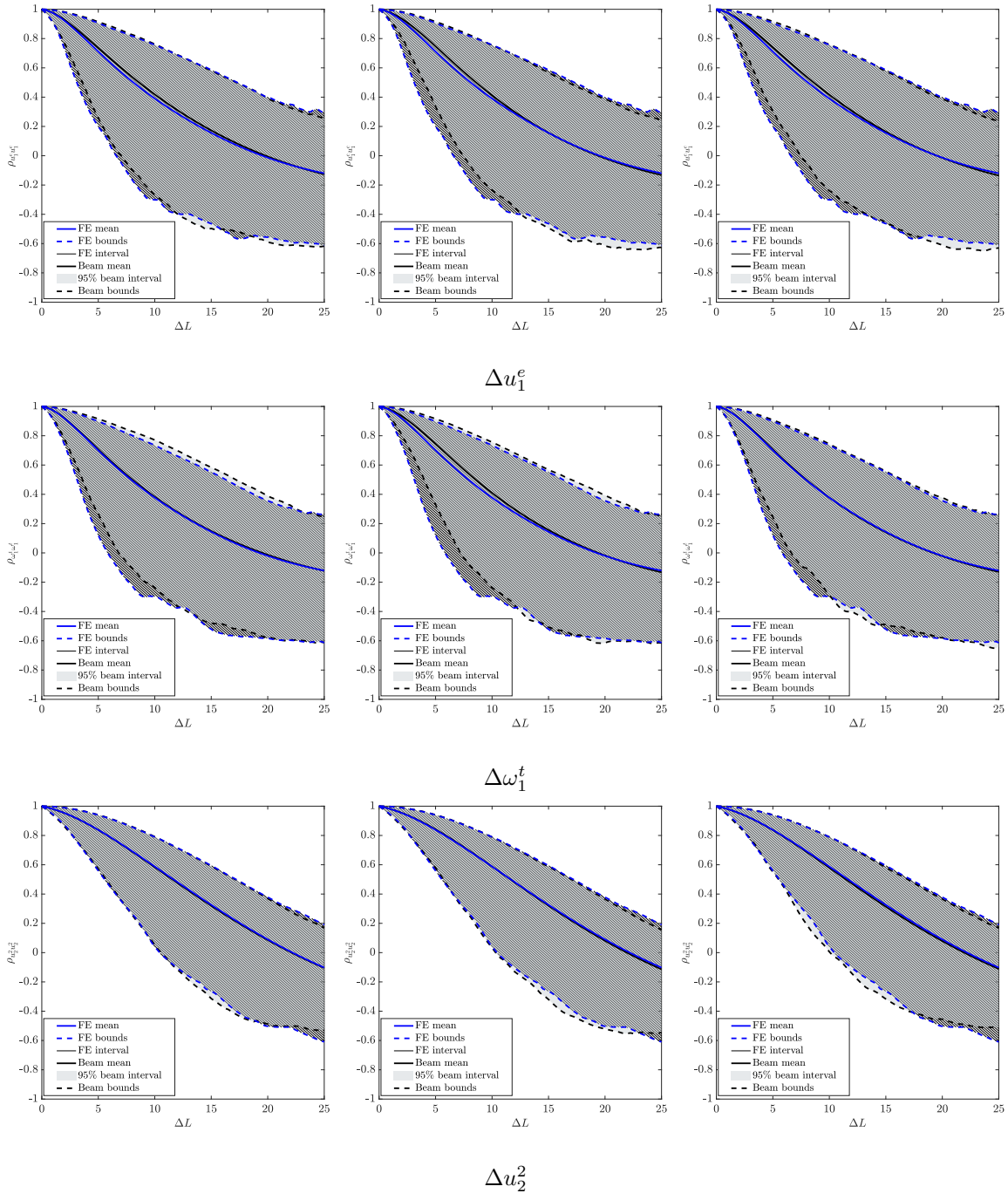

Figure 14: Prediction and observation intervals for the autocorrelation functions of both the FE and beam simulations alongside the means. Left: independent fields, center: ICM and right: SLFM. All predictions and observations are similar. However, based on the means for Δu_1^e and $\Delta \omega_1^t$, it is clear that the independent fields and SLFM are more accurate than the ICM approach. The ICM method yields wider prediction intervals, so that, with the exception for Δu_1^e and $\Delta \omega_1^t$, a larger portion of the FE results remains within its prediction intervals. Note that ΔL remains smaller than 25 to avoid unreasonable numerical errors.

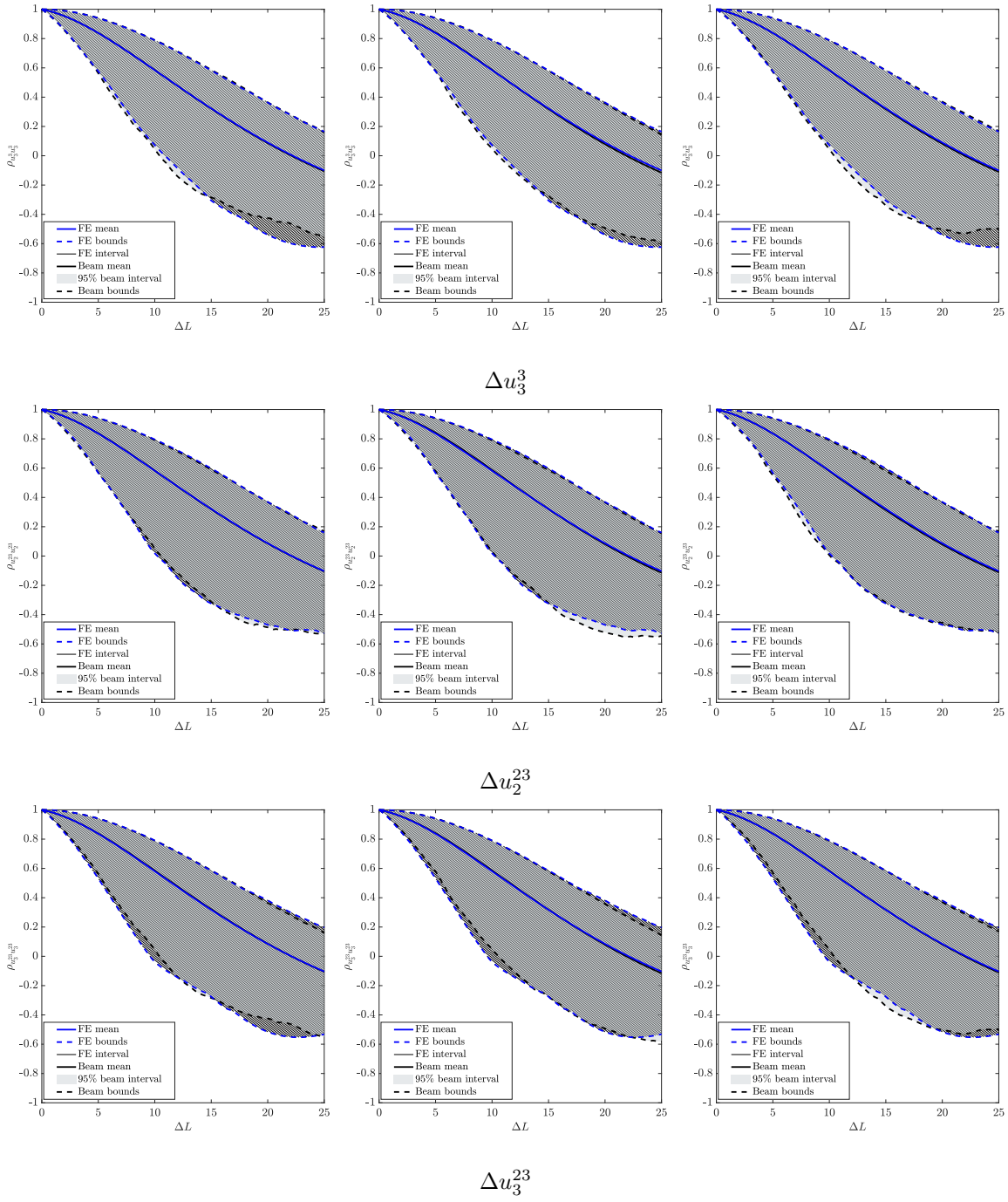

Continued Figure 14: Prediction and observation intervals for the autocorrelation functions of both the FE and beam simulations alongside the means. Left: independent fields, center: ICM and right: SLFM. All predictions and observations are similar. However, based on the means for Δu_1^e and $\Delta\omega_1^t$, it is clear that the independent fields and SLFM are more accurate than the ICM approach. The ICM method yields wider prediction intervals, so that, with the exception for Δu_1^e and $\Delta\omega_1^t$, a larger portion of the FE results remains within its prediction intervals. Note that ΔL remains smaller than 25 to avoid unreasonable numerical errors.

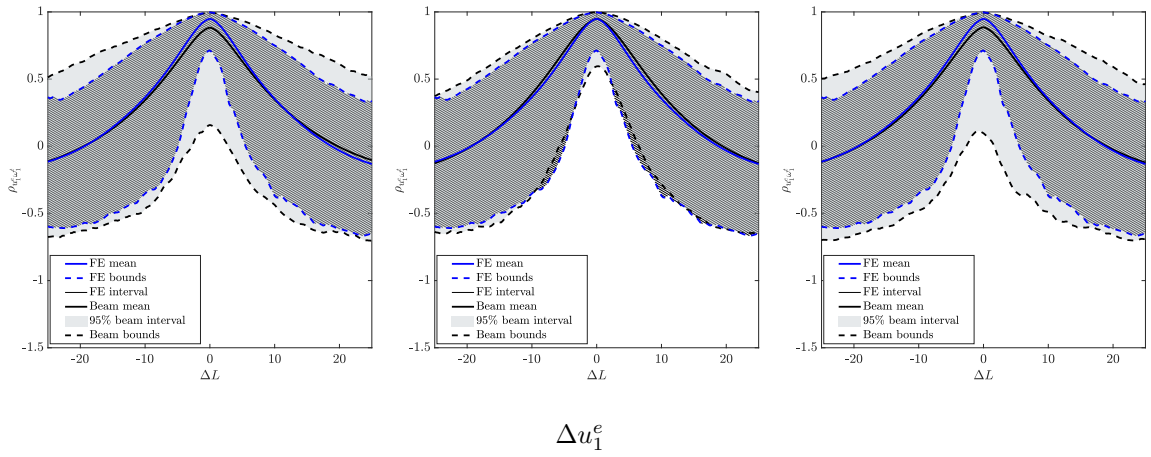

Figure 15: Prediction and observation intervals for the cross-correlation functions of both the FE and beam simulations alongside the means. Left: independent fields, center: ICM and right: SLFM. Only the cross-correlation function between Δu_1^e and $\Delta\omega_1^t$ is presented as the other cross correlations are the same for the three approaches. The envelopes of both the independent fields and the SLFM methods include the entire FE intervals. On the other hand, the mean cross-correlation of the ICM method is more accurate than those of both the independent fields and SLFM methods. Note that ΔL remains smaller 25 to avoid unreasonable numerical errors.

occasionally outside the prediction interval. Nevertheless, considering the mean cross-correlation function the ICM method performs better than both the independent fields and SLFM methods[5].

8. Conclusions

In this contribution, two formulations (i.e. the intrinsic coregionalization model and the semiparametric latent factor model) to describe the correlations between random fields are numerically investigated and compared to the case of independent fields (i.e. without correlation). The random fields are bounded so that bounds of the physical parameters are incorporated.

The identification of the random fields' parameters is hybrid: first, the spatially fluctuating parameters of each specimen are deterministically identified, and subsequently the random fields' parameters are probabilistically identified (using Bayesian inference). The probabilistic identification of the random fields' parameters is required because a limited number of specimens are available in practice.

The formulations and the identification of their parameters are applied to six hollow struts with random geometries. The geometry of each hollow strut is known and several mechanical tests are virtually applied to each strut geometry. The high accuracy of these simulations is achieved by representing each strut geometry with a detailed finite element discretization.

The results of the detailed tests are locally fluctuating center line displacements, as well as reaction forces and moments, which are to be described by an equivalent beam representation (since beam representations yield significantly more efficient simulations of entire strut networks). The input fields of the beam representations are the random fields' realizations of interest.

The results indicate that:

- The intrinsic coregionalization model leads to wider prediction intervals that contain all the finite element results, whereas the finite element results are occasionally outside the prediction intervals of the independent fields model and the semiparametric latent factor model.
- The independent fields model and the semiparametric latent factor model predict the finite elements' probability density functions of the reaction forces and moments slightly better.
- The probability density functions of the reaction forces and moments for all three approaches contain the finite elements' reaction forces and moments.

[5]Cross-correlation function is generally not symmetric and $\rho_{xy}(k) = \rho_{yx}(-k)$ (see [72]).

- The autocorrelation functions' mean estimators of both the independent fields model and the semiparametric latent factor model are better than those of the intrinsic coregionalization model. However, the intrinsic coregionalization model yields wider prediction intervals that contain more of the finite elements' results.
- The mean estimator of the intrinsic coregionalization model is better than the ones of the independent fields and semiparametric latent factor model. However, the prediction intervals for the independent fields model and the semiparametric latent factor model contain all the finite elements' results.

The linear elastic strut geometries are artificially generated, so that a numerical comparison between the 'true' struts and the beam representations is possible. In the future however, the strut geometries will be characterized by experimental techniques (and elastoplasticity will be used instead of linear elasticity), entailing that a comparison will not be possible.

Acknowledgements

Hussein Rappel was supported by Wave 1 of The UKRI Strategic Priorities Fund under the EPSRC Grant EP/T001569/1 and EPSRC Grant EP/W006022/1, particularly the "Digital twins for complex systems engineering" theme within those grants and The Alan Turing Institute. Mark Girolami acknowledges support from the UK Engineering and Physical Sciences Research Council (grant nos. EP/T000414/1, EP/R018413/2, EP/P020720/2, EP/R034710/1, EP/R004889/1), as well as a Research Chair supported by the Royal Academy of Engineering and Lloyds Register Foundation. Lars Beex gratefully acknowledges the financial support of the Fonds National de la Recherche Luxembourg for project *Open-cell Metal Foams* (Grant No. INTER/DFG/16/11501927; Funder ID: 10.13039/501100001866). The FE simulation results presented in this paper were carried out using the HPC facilities of the University of Luxembourg [73] – see `https://hpc.uni.lu`.

References

[1] A. Jung, L. Beex, S. Diebels, S. Bordas, Open-cell aluminium foams with graded coatings as passively controllable energy absorbers, Materials & Design 87 (2015) 36–41.

[2] A. Kulachenko, T. Uesaka, Direct simulations of fiber network deformation and failure, Mechanics of Materials 51 (2012) 1 –14.

[3] A. Dressler, E. Jost, J. Miers, D. Moore, C. Seepersad, B. Boyce, Heterogeneities dominate mechanical performance of additively manufactured metal lattice struts, Additive Manufacturing 28 (2019) 692–703.

[4] D. Page, F. El-Hosseiny, Mechanical properties of single wood pulp fibres. VI. Fibril angle and the shape of the stress-strain curve, Pulp & paper Canada.

[5] E. Gentleman, A. Lay, D. Dickerson, E. Nauman, G. Livesay, K. Dee, Mechanical characterization of collagen fibers and scaffolds for tissue engineering, Biomaterials 24 (21) (2003) 3805 –3813.

[6] H. Rappel, L. Wu, L. Noels, L. Beex, A Bayesian framework to identify random parameter fields based on the copula theorem and Gaussian fields: Application to polycrystalline materials, Journal of Applied Mechanics 86 (12), 121009.

[7] C. E. Rasmussen, C. K. I. Williams, Gaussian processes for machine learning, Vol. 1, MIT press Cambridge, 2006.

[8] D. J. C. MacKay, Information theory, inference and learning algorithms, Cambridge university press, 2003.

[9] A. Gelman, J. B. Carlin, H. S. Stern, D. B. Rubin, Bayesian data analysis, Chapman & Hall/CRC Texts in Statistical Science, Chapman & Hall/CRC, 2003.

[10] S. Rogers, M. Girolami, A first course in machine learning, second edition, 2nd Edition, Chapman & Hall/CRC, 2016.

[11] M. C. Kennedy, A. O'Hagan, Bayesian calibration of computer models, Journal of the Royal Statistical Society: Series B (Statistical Methodology) 63 (3) (2001) 425–464.

[12] M. Bayarri, J. Berger, R. Paulo, J. Sacks, J. Cafeo, J. Cavendish, C. Lin, J. Tu, A framework for validation of computer models, Technometrics 49 (2) (2007) 138–154.

[13] P. Arendt, D. Apley, W. Chen, Quantification of model uncertainty: Calibration, model discrepancy, and identifiability, Journal of Mechanical Design 134 (10) (2012) 100908.

[14] H. Rappel, L. A. A. Beex, L. Noels, S. P. A. Bordas, Identifying elastoplastic parameters with Bayes' theorem considering output error, input error and model uncertainty, Probabilistic Engineering Mechanics 55 (2018) 28–41.

[15] S. Jaimungal, E. K. H. Ng, Kernel based copula processes, in: W. Buntine, M. Grobelnik, D. Mladenić, J. Shawe-Taylor (Eds.), Machine Learning and Knowledge Discovery in Databases, Springer Science & Business Media, Berlin, Heidelberg, 2009, pp. 628–643.

[16] A. G. Wilson, Z. Ghahramani, Copula processes, in: Advances in Neural Information Processing Systems, 2010, pp. 2460–2468.

[17] R. B. Nelsen, An introduction to copulas, Springer Science & Business Media, 2007.

[18] P. X. Song, Multivariate dispersion models generated from Gaussian copula, Scandinavian Journal of Statistics 27 (2) (2000) 305–320.

[19] T. Haas, Multivariate spatial prediction in the presence of non-linear trend and covariance non-stationarity, Environmetrics 7 (2) (1996) 145–165.

[20] J. Ver Hoef, R. Barry, Constructing and fitting models for cokriging and multivariable spatial prediction, Journal of Statistical Planning and Inference 69 (2) (1998) 275 – 294.

[21] Y. Teh, W. Seeger, M. Jordan, Semiparametric latent factor models, in: AISTATS, 2005.

[22] E. Bonilla, K. Chai, C. Williams, Multi-task Gaussian process prediction, in: Advances in neural information processing systems, 2008, pp. 153–160.

[23] M. Álvarez, N. Lawrence, Computationally efficient convolved multiple output Gaussian processes, Journal of Machine Learning Research 12 (41) (2011) 1459–1500.

[24] P. Moreno-Muñoz, A. Artés, M. Álvarez, Heterogeneous multi-output gaussian process prediction, in: Advances in neural information processing systems, 2018, pp. 6711–6720.

[25] O. Hamelijnck, T. Damoulas, K. Wang, M. Girolami, Multi-resolution multi-task Gaussian processes, in: Advances in Neural Information Processing Systems, Vol. 32, Curran Associates, Inc., 2019, pp. 14025–14035.

[26] D. Higdon, J. Gattiker, B. Williams, M. Rightley, Computer model calibration using high-dimensional output, Journal of the American Statistical Association 103 (482) (2008) 570–583.

[27] S. Conti, J. Gosling, J. Oakley, A. O'Hagan, Gaussian process emulation of dynamic computer codes, Biometrika 96 (3) (2009) 663–676.

[28] S. Conti, A. O'Hagan, Bayesian emulation of complex multi-output and dynamic computer models, Journal of Statistical Planning and Inference 140 (3) (2010) 640–651.

[29] T. Fricker, J. Oakley, N. Urban, Multivariate Gaussian process emulators with nonseparable covariance structures, Technometrics 55 (1) (2013) 47–56.

[30] I. Bilionis, N. Zabaras, B. Konomi, G. Lin, Multi-output separable Gaussian process: Towards an efficient, fully Bayesian paradigm for uncertainty quantification, Journal of Computational Physics 241 (2013) 212–239.

[31] A. Gregory, F. Din-Houn Lau, M. Girolami, L. Butler, M. Elshafie, The synthesis of data from instrumented structures and physics-based models via Gaussian processes, Journal of Computational Physics 392 (2019) 248 –265.

[32] P. Arendt, D. Apley, W. Chen, D. Lamb, D. Gorsich, Improving identifiability in model calibration using multiple responses, Journal of Mechanical Design 134 (10), 100909.

[33] R. Richardson, M. Osborne, D. Howey, Gaussian process regression for forecasting battery state of health, Journal of Power Sources 357 (2017) 209–219.

[34] M. Álvarez, L. Rosasco, N. Lawrence, Kernels for vector-valued functions: A review, Foundations and Trends® in Machine Learning 4 (3) (2012) 195–266.

[35] L. Haitao, J. Cai, Y. Ong, Remarks on multi-output Gaussian process regression, Knowledge-Based Systems 144 (2018) 102–121.

[36] J. Isenberg, Progressing from least squares to Bayesian estimation, in: Proceedings of the 1979 ASME design engineering technical conference, New York, 1979, pp. 1–11.

[37] K. F. Alvin, Finite element model update via bayesian estimation and minimization of dynamic residuals, AIAA journal 35 (5) (1997) 879–886.

[38] J. L. Beck, L. S. Katafygiotis, Updating models and their uncertainties. I: Bayesian statistical framework, Journal of Engineering Mechanics 124 (4) (1998) 455–461.

[39] T. Marwala, S. Sibisi, Finite element model updating using Bayesian framework and modal properties, Journal of Aircraft 42 (1) (2005) 275–278.

[40] C. Gogu, R. Haftka, R. Le Riche, J. Molimard, A. Vautrin, Introduction to the Bayesian approach applied to elastic constants identification, AIAA journal 48 (5) (2010) 893–903.

[41] T. C. Lai, K. H. Ip, Parameter estimation of orthotropic plates by Bayesian sensitivity analysis, Composite Structures 34 (1) (1996) 29–42.

[42] F. Daghia, S. de Miranda, F. Ubertini, E. Viola, Estimation of elastic constants of thick laminated plates within a Bayesian framework, Composite Structures 80 (3) (2007) 461–473.

[43] J. M. Nichols, W. A. Link, K. D. Murphy, C. C. Olson, A bayesian approach to identifying structural nonlinearity using free-decay response: Application to damage detection in composites, Journal of Sound and Vibration 329 (15) (2010) 2995–3007.

[44] C. Gogu, W. Yin, R. Haftka, P. Ifju, J. Molimard, R. Le Riche, A. Vautrin, Bayesian identification of elastic constants in multi-directional laminate from moiré interferometry displacement fields, Experimental Mechanics 53 (4) (2013) 635–648.

[45] T. Most, Identification of the parameters of complex constitutive models: Least squares minimization vs. Bayesian updating, in: D. Straub (Ed.), Reliability and optimization of structural systems, CRC press, 2010, pp. 119–130.

[46] H. Rappel, L. Beex, J. Hale, L. Noels, S. Bordas, A tutorial on bayesian inference to identify material parameters in solid mechanics, Archives of Computational Methods in Engineering 27 (2) (2020) 361–385.

[47] Y. Zhang, J. Hart, A. Needleman, Identification of plastic properties from conical indentation using a Bayesian-type statistical approach, Journal of Applied Mechanics 86 (1).

[48] Y. Zhang, A. Needleman, Characterization of plastically compressible solids via spherical indentation, Journal of the Mechanics and Physics of Solids 148 (2021) 104283.

[49] M. Muto, J. L. Beck, Bayesian updating and model class selection for hysteretic structural models using stochastic simulation, Journal of Vibration and Control 14 (1-2) (2008) 7–34.

[50] P. Liu, S. K. Au, Bayesian parameter identification of hysteretic behavior of composite walls, Probabilistic Engineering Mechanics 34 (2013) 101–109.

[51] D. D. Fitzenz, A. Jalobeanu, S. H. Hickman, Integrating laboratory creep compaction data with numerical fault models: A Bayesian framework, Journal of Geophysical Research: Solid Earth 112 (B8), B08410.

[52] W. P. Hernandez, F. C. L. Borges, D. A. Castello, N. Roitman, C. Magluta, Bayesian inference applied on model calibration of fractional derivative viscoelastic model, in: V. Steffen Jr, D. A. Rade, W. M. Bessa (Eds.), DINAME 2015-Proceedings of the XVII International symposium on dynamic problems of mechanics, Natal, 2015.

[53] H. Rappel, L. A. A. Beex, S. P. A. Bordas, Bayesian inference to identify parameters in viscoelasticity, Mechanics of Time-Dependent Materials 22 (2) (2018) 221–258.

[54] H. Rappel, L. A. A. Beex, Estimating fibres' material parameter distributions from limited data with the help of Bayesian inference, European Journal of Mechanics - A/Solids 75 (2019) 169 – 196.

[55] M. Mohamedou, K. Zulueta, C. N. Chung, H. Rappel, L. A. A. Beex, L. Adam, A. Arriaga, Z. Major, L. Wu, L. Noels, Bayesian identification of mean-field homogenization model parameters and uncertain matrix behavior in non-aligned short fiber composites, Composite Structures 220 (2019) 64–80.

[56] P. S. Koutsourelakis, A multi-resolution, non-parametric, Bayesian framework for identification of spatially-varying model parameters, Journal of Computational Physics 228 (17) (2009) 6184–6211.

[57] P. S. Koutsourelakis, A novel Bayesian strategy for the identification of spatially varying material properties and model validation: An application to static elastography, International Journal for Numerical Methods in Engineering 91 (3) (2012) 249–268.

[58] F. Uribe, I. Papaiannou, W. Betz, J. Latz, D. Straub, Bayesian model inference od random fields represented with the Karahunen-Loève expansion, in: UNCECOMP 2017 2 nd ECCOMAS Thematic Conference on Uncertainty Quantification in Computational Sciences and Engineering, 2017.

[59] A. Vigliotti, G. Csányi, V. S. Deshpande, Bayesian inference of the spatial distributions of material properties, Journal of the Mechanics and Physics of Solids 118 (2018) 74–97.

[60] D. Savvas, I. Papaioannou, G. Stefanou, Bayesian identification and model comparison for random property fields derived from material microstructure, Computer Methods in Applied Mechanics and Engineering 365 (2020) 113026.

[61] L. Beex, P. Kerfriden, T. Rabczuk, S. Bordas, Quasicontinuum-based multiscale approaches for plate-like beam lattices experiencing in-plane and out-of-plane deformation, Computer Methods in Applied Mechanics and Engineering 279 (2014) 348–378.

[62] P. Michaleris, D. Tortorelli, C. Vidal, Tangent operators and design sensitivity formulations for transient non-linear coupled problems with applications to elastoplasticity, International Journal for Numerical Methods in Engineering 37 (14) (1994) 2471–2499. arXiv:https://onlinelibrary.wiley.com/doi/pdf/10.1002/nme.1620371408.

[63] W. Wenjia, P. Clausen, K. Bletzinger, Efficient adjoint sensitivity analysis of isotropic hardening elastoplasticity via load steps reduction approximation, Computer Methods in Applied Mechanics and Engineering 325 (2017) 612 – 644.

[64] M. Sklar, Fonctions de répartition à n dimensions et leurs marges, Université Paris 8, 1959.

[65] Y. Noh, K. K. Choi, I. Lee, Identification of marginal and joint CDFs using Bayesian method for RBDO, Structural and Multidisciplinary Optimization 40 (1) (2009) 35.

[66] S. Brooks, A. Gelman, G. Jones, L. X. Meng, Handbook of Markov chain Monte Carlo, CRC press, 2011.

[67] J. L. Beck, Bayesian system identification based on probability logic, Structural Control and Health Monitoring 17 (7) (2010) 825–847.

[68] Y. Dai, Y. Yuan, A nonlinear conjugate gradient method with a strong global convergence property, SIAM Journal on Optimization 10 (1) (1999) 177–182. arXiv:https://doi.org/10.1137/S1052623497318992.

[69] H. Haario, E. Saksman, J. Tamminen, Adaptive proposal distribution for random walk Metropolis algorithm, Computational Statistics 14 (3) (1999) 375–396.

[70] M. Singull, M. Ahmad, D. von Rosen, More on the Kronecker structured covariance matrix, Communications in Statistics - Theory and Methods 41 (13-14) (2012) 2512–2523.

[71] W. Edwards, H. Lindman, L. Savage, Bayesian statistical inference for psychological research., Psychological review 70 (3) (1963) 193.

[72] G. Box, G. Jenkins, G. Reinsel, G. Ljung, Time series analysis: Forecasting and control, Wiley Series in Probability and Statistics, Wiley, 2015.

[73] S. Varrette, P. Bouvry, H. Cartiaux, F. Georgatos, Management of an academic HPC cluster: The UL experience, in: Proc. of the 2014 Intl. Conf. on High Performance Computing & Simulation (HPCS 2014), IEEE, Bologna, Italy, 2014, pp. 959–967.